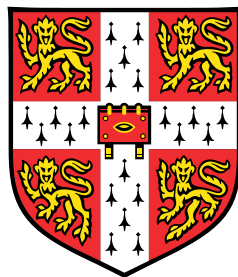


Multi-Dimensional Electron Diffraction in Pharmaceutical Materials

1st Year Report



Helen Leung

Department of Materials Science and Metallurgy
University of Cambridge

This dissertation is submitted at the end of the 1st year of
Doctor of Philosophy

Acknowledgements

I would like to thank my academic supervisor, Paul Midgley, and my industrial supervisors, Roy Copley and Duncan Johnstone for the guidance and support that I have received. I also thank the other members of the electron microscopy group, in particular Petr Vacek and Joonatan Laulainen, for providing scientific advice and for training me on the microscopes. In addition, I would like to acknowledge the funding I receive through the Engineering and Physical Sciences Research Council, as well as from GSK.

Abstract

In the pharmaceutical industry, an understanding of both the molecular structure and the microstructure of potential assets holds the key to controlling their physical and chemical properties. To characterise these properties, the current ‘gold standards’ used by the industry are X-ray diffraction, nuclear magnetic resonance, and other bulk characterisation techniques. However, these techniques lack the ability to probe a sample on the nanoscale. Electron beams can be focussed into nano-meter sized probes which means they can be used to study samples at much higher spatial resolution. Scanning electron diffraction involves the acquisition of a diffraction pattern at each probe position in real space using a converged beam. It is a powerful technique which can reveal nano-structures and identify areas of nanocrystallinity which may enhance understanding of some solid-state questions which are key to the industry. In comparison, 3-dimensional electron diffraction involves the acquisition of a tilt series from a crystallite which enables crystallographers to solve and refine crystal structures of small organic molecules and macromolecules such as proteins. Both of these techniques are able to reveal a wealth of structural information about a sample.

In this report, the potential for the application of electron diffraction techniques within the pharmaceutical industry is reviewed, alongside the main areas for development. As an example of such an application, scanning electron diffraction is used to study a pharmaceutical amorphous solid dispersion. Then, the use of the multislice method for dynamical simulations of small tilt electron diffraction patterns is attempted and discussed.

Table of contents

1	Introduction	1
1.1	Materials Characterisation in the Pharmaceutical Industry	1
1.1.1	Drug Discovery: Structure Determination	3
1.1.2	Drug Manufacturing: Probing Microstructure	5
1.2	Sample Product Classes	8
1.3	Overview and Motivations	10
2	Electron Diffraction Theory	11
2.1	Electron Diffraction	11
2.1.1	Acquisition Modalities in Electron Diffraction	12
2.1.2	Scanning Electron Diffraction	12
2.1.3	Precession Electron Diffraction	13
2.1.4	3D Electron Diffraction (MicroED)	15
2.1.5	Serial Electron Diffraction	17
2.2	Key Challenges of Electron Diffraction	18
2.2.1	Kinematical vs Dynamical Diffraction	18
2.2.2	Large Unit Cells	21
2.2.3	Beam-Sensitivity	21
2.3	Analysis of Electron Diffraction Data	23
2.3.1	SED Data: Probing Microstructure	23
2.3.2	3D-ED Data: Solving Crystal Structures	24
2.3.3	TEM Sample Preparation	28
3	Amorphous Solid Dispersions	29
3.1	Literature Review	29
3.1.1	Factors Affecting Crystallinity in ASDs	30
3.1.2	Manufacturing Methods for ASD Synthesis	31

3.1.3	Indomethacin - PVP: a continuation of a previous study within the group	31
3.2	Method	35
3.2.1	Experimental Methods	35
3.2.2	Data Processing	37
3.3	Results and Discussion	40
3.3.1	Pure Indomethacin Crystals	40
3.3.2	Indomethacin-PVP ASDs	40
3.3.3	Varying Reported Solubility Limits	51
3.4	Improving the work	53
3.4.1	Further XRD analysis	53
3.4.2	Increasing Data Quality	53
3.4.3	Developing Diffraction Pattern Analysis	54
3.5	Conclusion and Outlook	54
4	Simulating Dynamical Diffraction	55
4.1	Image Simulation Theory	55
4.2	Motivations: Diffraction Simulation in Organic Crystals	57
4.3	Method	57
4.4	Results and Discussion	59
4.5	Conclusion	61
5	Future Work	63
5.1	Microstructure and Structure Solution in Solid Form	63
5.1.1	Structure Determination of τ Polymorph	63
5.1.2	Defect Analysis in Organic Crystals	63
5.2	SED of Long Acting Injectables	64
5.3	Dynamical Bloch Wave Simulations	64
5.4	Technique Development	65
5.4.1	Machine Learning for High Throughput Data Processing	65
5.4.2	Precession	65
References		67

Chapter 1

Introduction

1.1 Materials Characterisation in the Pharmaceutical Industry

Small organic molecules constitute the majority of the active pharmaceutical ingredients (APIs) produced by the pharmaceutical industry. In 2020, they made up 71% of all FDA-approved drugs [110]. Both the molecular and crystal structure of these pharmaceutical compounds control vital properties such as its toxicity, stability, and solubility which are vital to understanding how a compound will perform in the body and during manufacture. An understanding of molecular connectivity in a drug is crucial to it being safe to use and this knowledge is needed given the highly regulated nature of the industry.

APIs are combined with excipients which are required to stabilise the compound and control other desirable physical properties which are key to the performance of the drug. Currently, a range of complementary techniques such as nuclear magnetic resonance (NMR), mass spectroscopy, and single crystal X-ray diffraction (SCXRD), are used for API structure determination which is needed in the drug discovery phase. Then, bulk characterisation techniques such as imaging, spectroscopy, powder X-ray diffraction (PXRD) and thermal analysis are used to investigate solid form questions about a sample product. For example, to understand its chemical and physical stability, or to understand its mechanical behaviour under a range of conditions: both of which may be dependent on the excipient used. This is crucial to the drug development phase.

Electron diffraction (ED) is a technique within the field of electron microscopy which is able to study a sample at a higher spacial resolution than bulk characterisation techniques allow. This can reveal local nano-crystalline structure which is key to understanding the solid state behaviour that is crucial in product formulation. In addition, electron beams can be used to solve molecular structures in

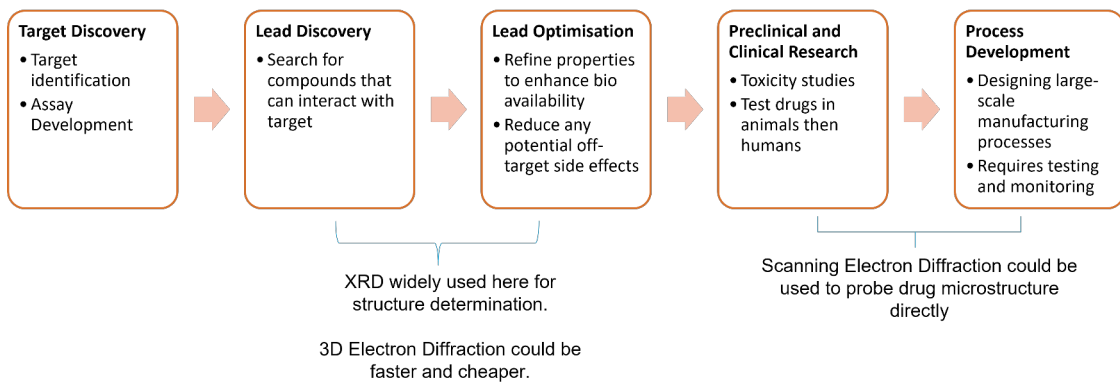


Fig. 1.1 A brief summary of the drug discovery pipeline: adapted from [14].

nanocrystals with much smaller sample volumes than would be possible with other techniques. There are many acquisition modalities which allows for a range of information to be collected and therefore a range of applications across the drug discovery pipeline. This pipeline is illustrated in Figure 1.1, where the stages for application of ED have been highlighted.

In the past, pharmaceutical applications of electron diffraction have been hampered primarily due to limitations in detectors. For many years, charge-coupled detectors (CCDs) were widely adopted in electron microscopy. In these detectors, high energy electrons are converted into photons within an electron scintillator, which are then guided to the CCD array using fiber optical couplings. These photons are converted back into low energy electrons and read out as a current. This method results in slow read-out speeds (ca. 1-100 fps) which are unable to meaningfully record signal from beam-sensitive materials (organic structures cannot withstand doses of more ca. 1 - 100 electrons per \AA^2 before losing crystallinity). The advent of direct-electron detectors, in which the use of photons as an intermediary is eliminated, allows for readout speeds of ca. 100-1000 fps [7]. In addition, ease of access to increased computing power has enabled the automated acquisition of vast amounts of data from the electron microscope in short spaces of time, which reduces the electron dose that a sample needs to be exposed to. The difference between these detectors is shown in Figure 1.2.

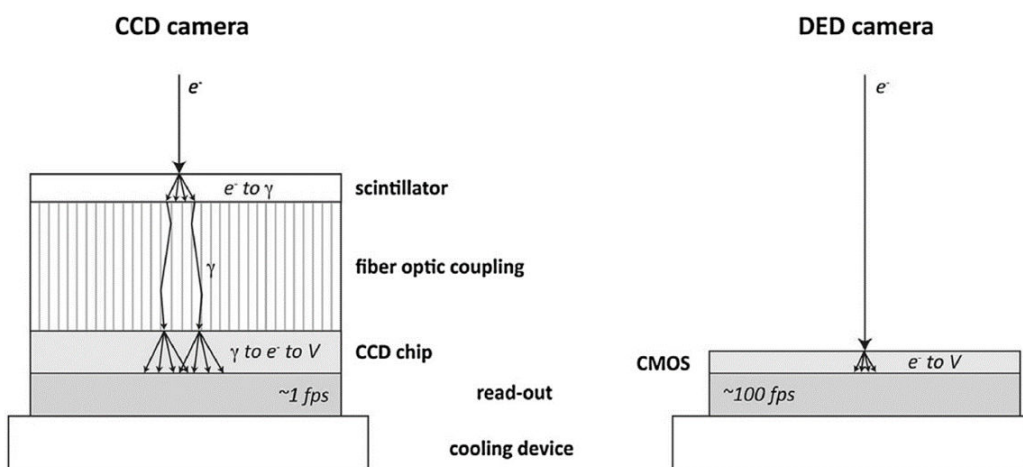


Fig. 1.2 Charge Coupled Device vs a Direct Electron Detector. Figure reproduced from [52].

1.1.1 Drug Discovery: Structure Determination

Drug discovery relies on understanding the structure of compounds of interest in order to optimise their properties and identify their potential as candidates. In principle, electron diffraction can be used for molecular structure determination and thus offers an alternative method to XRD and NMR to enable drug discovery.

The Status Quo: X-ray Diffraction (XRD)

Currently, X-ray diffraction (XRD) is widely recognised as the industrial gold standard for structure and phase determination of APIs. However, there are several disadvantages of using XRD in the pharmaceutical context. Single crystal X-ray diffraction (SCXRD), which is used for molecular structure determination, requires that samples are large single crystals of micron dimensions. Growing single crystals large enough for SCXRD is often not possible due to the instability or scarcity of a compound. Where single crystal growth is possible, the process can take between several days and months to obtain crystals of sufficient quality [93].

Rather than using a single crystal, X-ray powder diffraction (PXRD) is a bulk characterisation technique used to reveal the crystallographic structure of a polycrystalline sample whose grain size is typically on the order of 10 - 50 μm [83]. However, it is difficult to determine information about the unit cell of the compound in unknown samples with multiple phases and preferred crystallite orientations. In addition, the probing volumes in lab-based X-ray diffraction are too large to obtain local crystallographic information because the signals from a large number of crystals (if they are smaller than 50 μm in

each dimension [31]) are averaged. Crystals of this size would produce overlapping signals causing data from potentially different phases or crystallite orientations to be indistinguishable. To investigate on the nanoscale, samples must be sent to centralised facilities such as synchotrons which provide the brightest X-ray sources with smaller probing volumes that are able to probe crystals on the order of 5-10 μm in each dimension [31]. In optimal circumstances, synchotrons have been shown to display limits of detection of 0.1% [73]. However, use of centralised facilities further increases the time required for structure determination. In organic materials, which have large and complex unit cells, peak overlap can be further exacerbated by the presence of defects, making PXRD data very hard to interpret. Therefore, this technique is unforgiving to the presence of impurities and texture in the microstructure.

Advantages of electron diffraction over X-ray diffraction

In comparison to X-rays, electrons have a much stronger interaction with the crystal structure due to their Coulombic interactions. Electromagnetic coils can be used to focus the electron beam into nano-meter sized probes which allows ED to access ‘sub-volumes’ of a sample, such as single crystals which are embedded in a matrix, or where there are several phases present in close proximity. In this way, ED can probe crystals 10^6 times smaller in volume than those required for XRD [57]. This means it can be used not only to study samples where only a small volume is available, but ED also offers local crystallographic information at much higher spatial resolutions. This comparison is illustrated in Figure 1.3.

Diffracting differently

With 3D electron-diffraction data and refinement using dynamical theory, a complete crystal structure with detail similar to that obtained with x-ray diffraction data from a crystal 1 million times larger can be achieved.

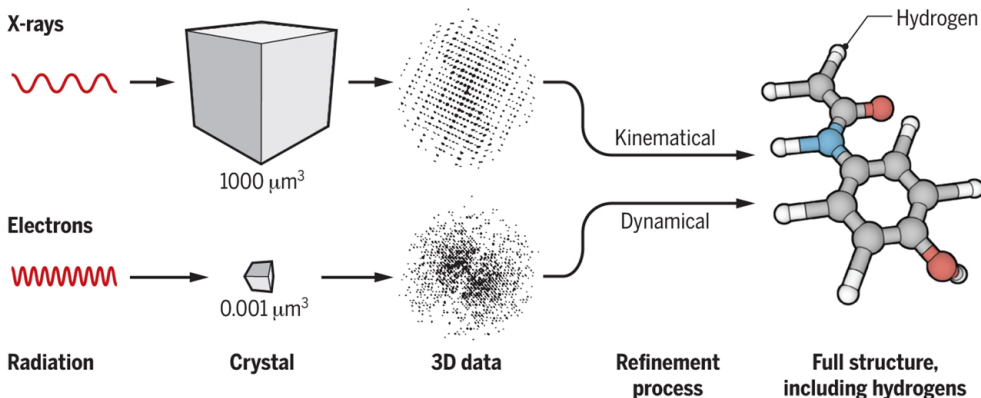


Fig. 1.3 Electrons can be used to probe a much smaller sample size: ideal for APIs which are hard to grow into large crystals. Figure reproduced from [64].

In addition, reciprocal and real space data can be simultaneously obtained. The combination of both diffraction and image data from a single region can be combined to enhance data acquisition and analysis; for example to track specific crystals of interest.

Another example of an advantage of electron diffraction would be in co-crystals. Co-crystals are a compound class of particular interest to the pharmaceutical industry due to their ability to modify physical properties of APIs. In addition, they offer another route for delivery of insoluble compounds into the body, as well as potential for improved mechanical properties of drug products [44]. However, distinguishing between co-crystals and salts relies on knowledge to high spatial accuracy of hydrogen positions. The transfer of the H⁺ ion creates a salt, whereas if the transfer has not occurred, the substance is classified as a cocrystal, as shown in Figure 1.4. This is important for regulation purposes. It is difficult to accurately locate H atoms using XRD structure refinement. However, electron diffraction can be used to tackle this problem due to the stronger Coulombic interaction of electrons. This makes the technique more sensitive to light elements such as H [77]. This is demonstrated by the structure solution of a co-crystal of sofobusvir and L-proline (an amino acid) by Brazda et al. [9].

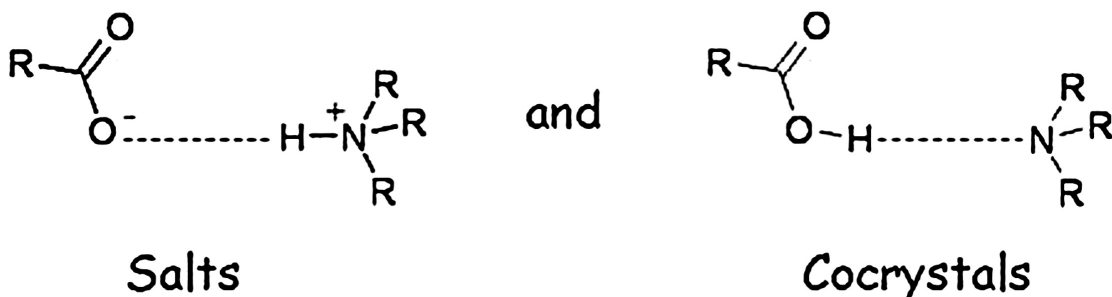


Fig. 1.4 Salts and co-crystals are different based on the position of H which as a result may alter other bond lengths too. Light atoms are very hard to place correctly in XRD. Figure reproduced from [25].

1.1.2 Drug Manufacturing: Probing Microstructure

Crystals used for structure determination with XRD are typically grown in carefully curated environments to control crystal growth for optimum sample quality. In reality, dependent on their varying properties, APIs will require a wide range of delivery mechanisms based on their optimised dosage forms that may not accurately reflect the crystals from which XRD structure is determined. Manufacturing APIs at scale can introduce questions about solid form [28]. Aside from structure determination, ED could also explore microstructural variations, such as to identify minority phases, impurities, and transformations that may have occurred within nano-volumes of a sample. The microstructure is important to the way that the crystal structure of a material affects its properties at different length scales. This is

important in drug manufacturing to understand the behaviour of the final marketed dosage form of a drug.

It is possible that the crystal structure in localised areas of a product may have changed from its original form: such as via process-induced phase transformations [53]. For example, ball-milling, which is a process used to micronise compounds to make nano-milled products, can lead to mechanochemical phase changes to other polymorphs in localised areas of a sample. Known examples of this include transformations in theophylline, lactose, and chlorpropamide [22]. Polymorphs are substances which have the same absolute molecular structure, but a different crystal packing which may alter many properties of the drug. As an example, Figure 1.5 shows two different polymorphs of acetaminophen, one with a monoclinic crystal structure, and the other with an orthorhombic crystal structure.

Polymorphs of a drug will have altered kinetic, surface, mechanical, packing, and thermodynamic properties [22]. This may affect what excipients are appropriate to use with the drug, and the form in which it can be stably administered. For example, ritonavir drug capsules were found to routinely fail dissolution tests due to a more thermodynamically stable (and therefore less soluble) polymorph of ritonavir precipitating during formulation and processing of the tablets [4].

The specific modalities within ED which would suit applications in drug discovery and drug development are discussed in Chapter 2.1.

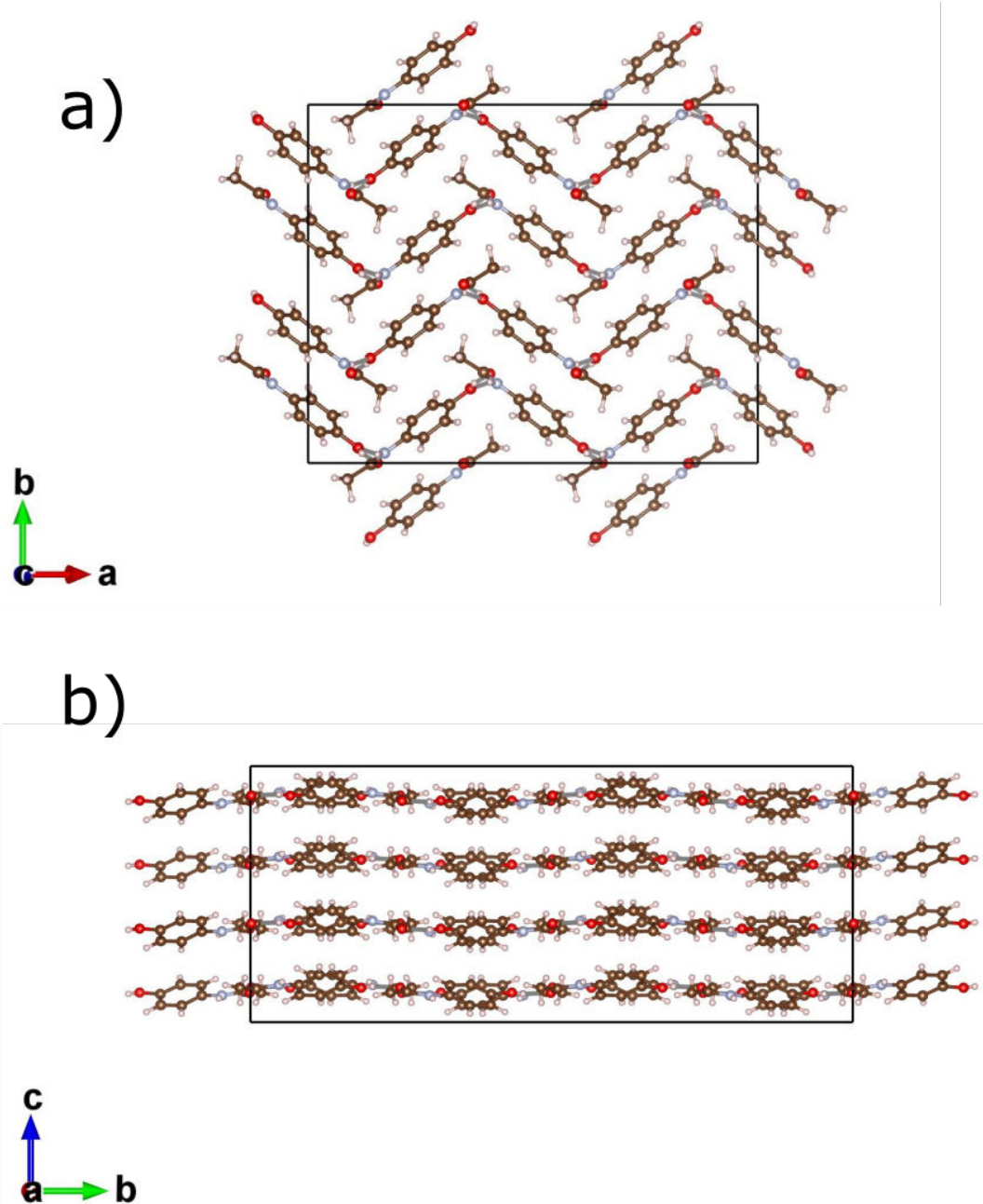


Fig. 1.5 An example of polymorphism in acetaminophen. a) Form 1 of acetaminophen which displays a herringbone structure. It has a monoclinic crystal structure. b) Form 2 of acetaminophen. It is metastable and has an orthorhombic crystal structure.

1.2 Sample Product Classes

In this section, common solid sample product classes which dominate the pharmaceutical market and are of interest to this report are summarised. The potential for application of ED to these products is discussed.

Tablets

Some tablets can be formed using direct compression. Flow properties of powders are important for manufacturing because particles are poured into dies before being compressed. Granulation may be used to agglomerate particles so that fine powders can be processed in a dust-free manner and compacted efficiently [80]. Agglomeration can happen via several mechanisms such as sintering, chemical reactions, and crystallisation. This requires careful monitoring of API structure, to ensure that the drug product has not been altered during processing, especially where use of heat has been involved. As an example of this, wet granulation was found to cause a polymorphic transformation of fexofenadine hydrochloride, an antihistamine. [95].

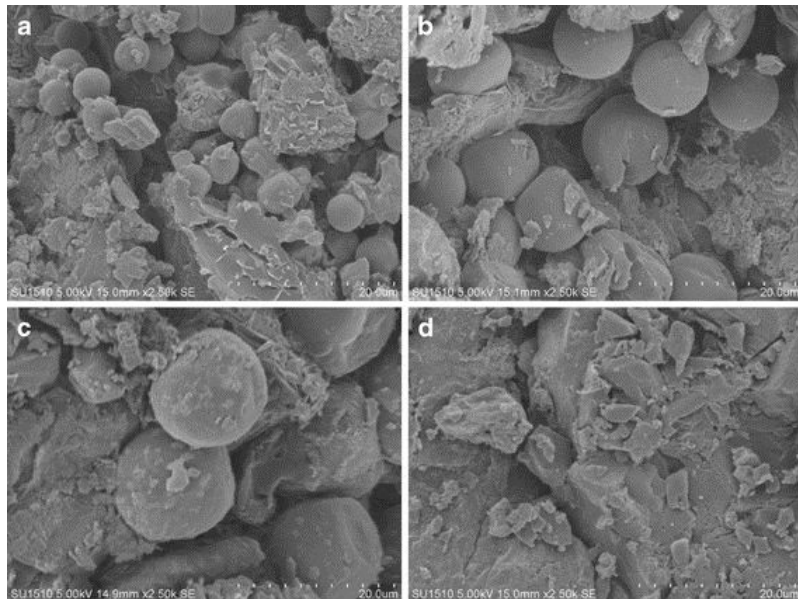


Fig. 1.6 SEM micrographs of tablet cross-sections to observe particle sizes at a local scale. a) - c) contain different sized polystyrene microspheres (5 – 15 μm) whilst a tablet with ebastine (the API of interest) is shown in d) [54]. Differences in morphology are evident but the crystal structure is not distinguishable without transmission electron microscopy.

Work by Kuriyama et al. [54] have shown the possibilities of producing tablet cross-sections for SEM (as shown in Figure 1.6). This was done by securing each tablet in an epoxy resin solution, then curing the resin. The tablet was then microtomed to reveal its interior surface. Electron diffraction could be

used to locate and identify potential changes in crystallinity. However, producing thin enough samples for transmission electron microscopy (TEM) without significantly altering the microstructure remains a challenge.

Long Acting Injectables

Long acting injectables (LAIs) are a type of parenteral. Parenterals are drugs which use non-oral means of administration, for example by injection. LAIs contain nanoparticles (with sizes of ca. 200 nm) which are designed to allow for slow release of the API in the body, as shown in Figure 1.7. Their properties are monitored primarily using bulk techniques which yield knowledge of LAIs on a macroscale [84]. However, electron diffraction could provide the high spatial resolution needed to probe these nanosuspensions on a local scale [38].

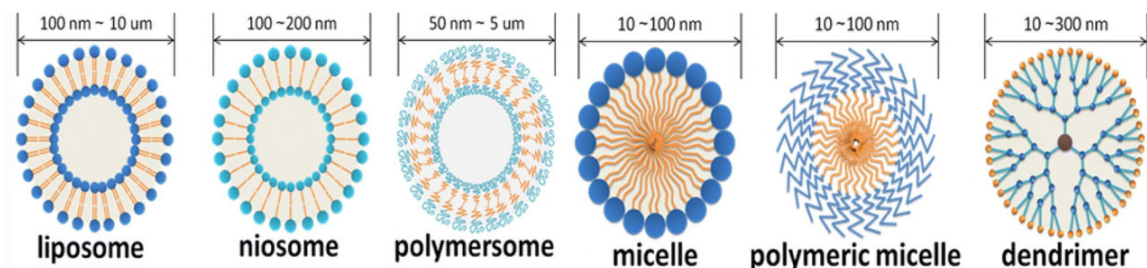


Fig. 1.7 LAIs contain nanoparticles which have been designed for slow release. Various nanovehicles can be used as shown. Drug release rates may be modified by controlling stability and permeability of these vehicles. Figure reproduced from [47].

Solid Dispersions

The oral bioavailability of an API relies on its aqueous solubility in gastric and intestinal fluids. Compounds of pharmaceutical interest are sometimes hydrophobic, forming crystalline phases which results in low *in vivo* efficacy. In solid dispersions, the API of interest is mixed with a water-soluble polymer [94] to improve its solubility. Shelf-life issues can arise due to unwanted API crystallinity forming over time.

The majority of solid dispersion characterisation has been done using XRD, NMR, and differential scanning calorimetry (DSC). In 2021, S'ari et al. showed that conventional transmission electron microscopy (CTEM) could be used to identify areas of the dispersion where the API had crystallised [96]. In this way, they were able to enhance understanding of the recrystallisation process in the solid dispersion under different conditions of humidity. An investigation of amorphous solid dispersions is the focus of the work presented in Chapter 3.

1.3 Overview and Motivations

This report focusses on the uses of ED for solid form and structure determination of small organic molecules in the pharmaceutical industry. Although macromolecules are also within the potential of ED ([70], [17]), effects such as dynamical diffraction require a greater understanding. The development of ED in small organic molecules will lay the foundations for robust application of this technique in macromolecules. ED will be a powerful complementary technique to the pre-existing methods used in the industry.

The rest of the report is structured as follows: in Chapter 2, a literature review of electron diffraction in beam sensitive materials is conducted, and the mechanics of different modes of acquisition are explained. In Chapter 3, experimental work carried out an amorphous solid dispersions is reported. In Chapter 4, attempts to simulate dynamical diffraction patterns are described, and in Chapter 5, future work that leads on from this report is detailed.

Chapter 2

Electron Diffraction Theory

2.1 Electron Diffraction

The transmission electron microscope (TEM) was invented in 1931 by Ruska [49]. In the TEM, an incident electron beam interacts with the atoms in a thin sample. These electrons can elastically scatter and produce a signal measured in electron diffraction. The unit cell dimensions will determine the positions of the diffracted beams of electrons, whilst the ordering of atoms within the unit cell will determine their intensities. Electron diffraction from crystalline structures is a particularly powerful signal because it can be used to determine quantities such as structure, orientation, defects, and strain. Advances in computing power and the development of direct electron detectors has broadened the use of transmission electron microscopy in recent years, especially within organic materials which are very sensitive to damage due to electron irradiation.

Diffraction geometry can be visualised in reciprocal space using the Ewald sphere construction, as shown in Figure 2.1. The intersection of the sphere's surface with reciprocal lattice points represent all elastically scattered wave-vectors which satisfy Bragg's law:

$$n \lambda = 2 d \sin \theta \quad (2.1)$$

where d is the interplanar spacing, λ is the wavelength of incoming radiation, θ is the incident angle between the incident ray and the scatter plane, and n is an integer. Each point in reciprocal space represents a set of hkl planes.

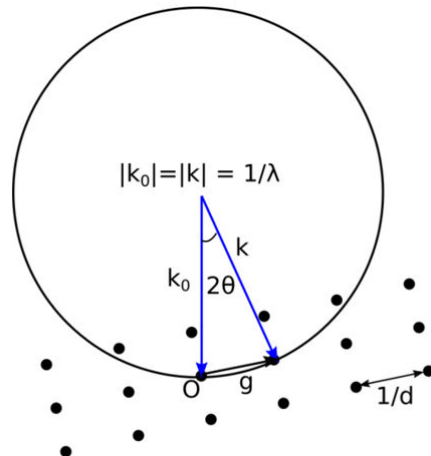


Fig. 2.1 The Ewald sphere construction. Figure taken from [37].

2.1.1 Acquisition Modalities in Electron Diffraction

There are several different ways that the electron beam in a TEM can be used to generate electron diffraction data. Each method offers ways to investigate different aspects of a sample. The modalities which are the focus of this work are: scanning electron diffraction (SED) [23]; 3D electron diffraction (3D-ED) [29]; precession electron diffraction (PED) [105], and serial rotation electron diffraction (SerialRED) [100]. Other diffraction techniques such as selected area ED (SAED), convergent beam ED (CBED), and low angle convergent beam ED (LACBED) are not discussed in this work.

2.1.2 Scanning Electron Diffraction

Scanning electron diffraction (SED, also known as 4D-STEM) is a technique whereby a convergent beam is raster-scanned across a sample area (ca. $1 \mu\text{m} \times 1 \mu\text{m}$). At each probe position, a diffraction pattern is recorded typically totalling 10^5 diffraction patterns per scan, as shown in Figure 2.2. This creates a ‘4-Dimensional’ dataset of spatially resolved diffraction patterns which contains information in both real and reciprocal space and can be used for powerful *post-facto* data analysis [23], even from beam sensitive samples. The convergence semi-angle of the electron beam is typically 0.5 - 1 mrad, and the probe size may be diffraction limited if the effects of lens aberrations (defocus, coma, astigmatism) can be eliminated effectively by correct beam alignment. The diameter of the probe, d , is expressed as:

$$d = \frac{1.22 \lambda}{\alpha} \quad (2.2)$$

where λ is the wavelength of illuminating radiation, and α is the convergence semi-angle. To keep up with the scanning probe, detectors with rapid read-out speeds are required to capture the data.

Cryo-EM has been the driving force behind the development of direct electron detectors which are capable of this task. The Merlin Medipix camera is a direct electron detector in which each pixel has its own independent readout electronics allowing for rapid readout speeds. There are two different possible modes of operation: single-pixel mode and charge summing mode. In single pixel mode, the threshold voltage is compared to the voltage signal from each pixel which is proportional to the charge collected. If the threshold is exceeded, the signal from a given pixel is recorded as an event [81]. The performance of detectors can be characterised by their Point Spread Function (PSF), Modulation Transfer Function (MTF), or Detector Quantum Efficiency (DQE) [92]. The PSF is a measurement of the energy spread of the detector and the MTF is the Fourier transform of this. The DQE indicates how many of the incoming electrons are successfully detected.

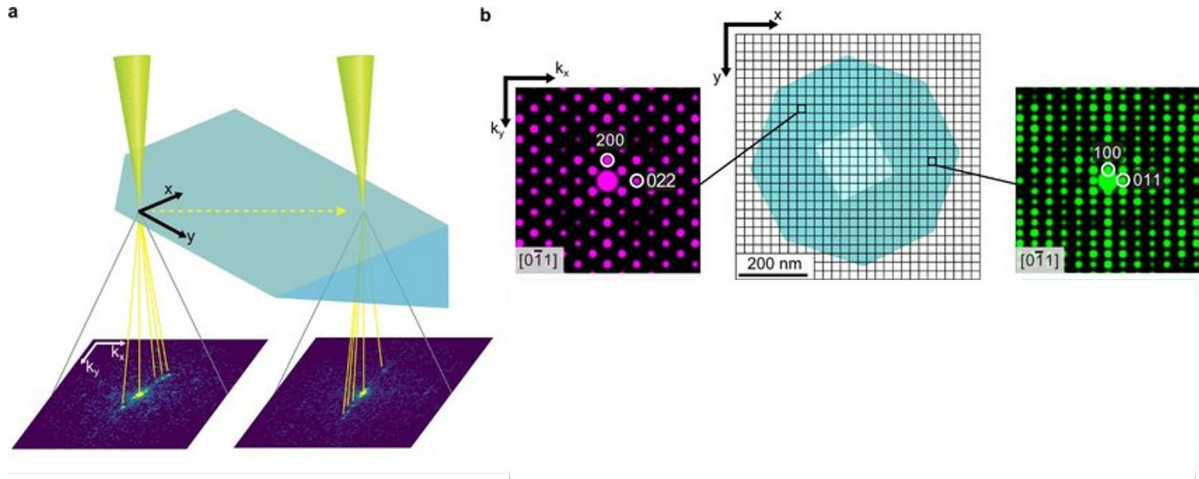


Fig. 2.2 SED. a) the beam is raster scanned across the sample. b) at each pixel in the resulting image, a diffraction pattern has been recorded. Figure reproduced from [40].

2.1.3 Precession Electron Diffraction

Precession electron diffraction (PED) is a technique which involves the conical rotation of the electron beam during data acquisition, and is the electron analogue of X-ray precession diffraction [10]. It was first developed by Midgley and Vincent [105]. The effect of precession is to minimise multi-beam dynamical effects by an integration of the diffracted intensity through the Bragg condition. This enables the ensemble of intensities in the pattern to be treated as if they were kinematical and thus enables easier location of the global minimum in any structural refinement, which is discussed in Section 2.3.2. In addition, the rocking motion of the beam (illustrated in Figure 2.3), leads to more reflections intercepting the Ewald Sphere, leading to more diffraction spots appearing in the data.

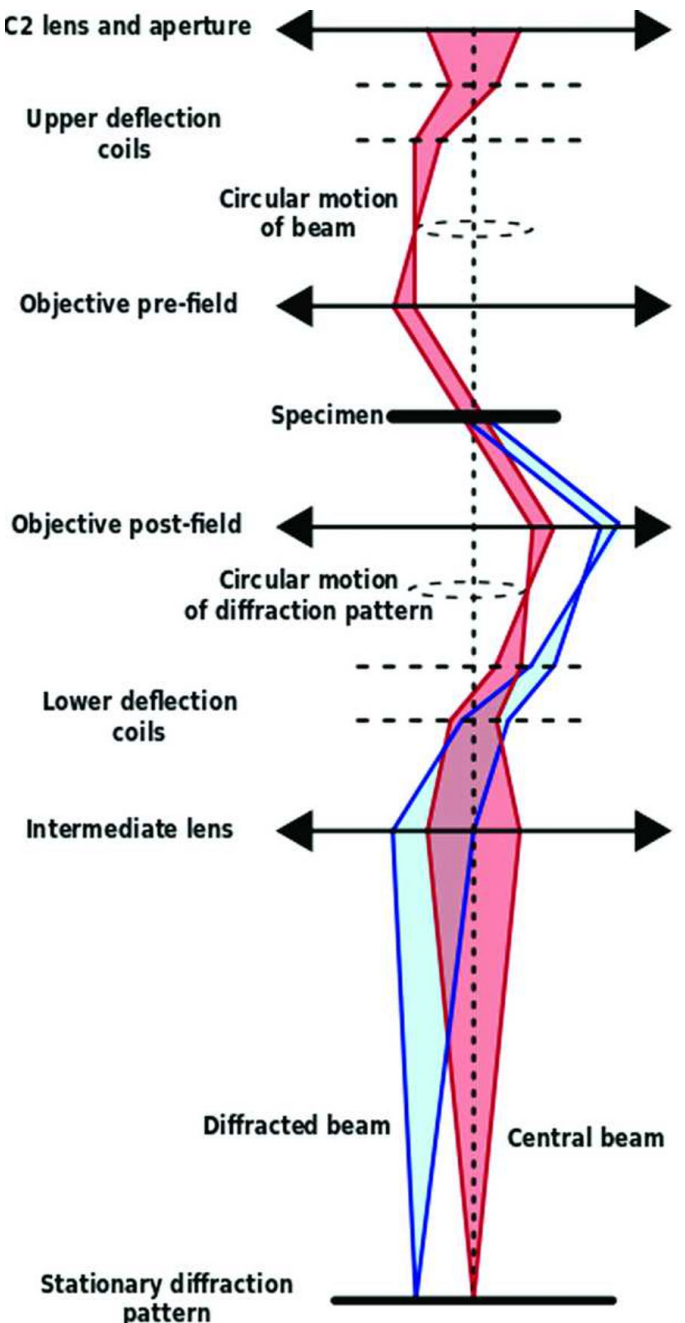


Fig. 2.3 Illustrating the geometry of beam movement during precession. Upper and lower deflection coils produce the circular motion of the beam and correct this motion post-specimen respectively. Figure reproduced from [65].

2.1.4 3D Electron Diffraction (MicroED)

In 3D Electron Diffraction (3D-ED), the sample is tilted around a range of angles using the microscope goniometer. At each tilt angle, a diffraction pattern is acquired. As a result, a series of patterns (called a tilt series) is captured (shown in Figure 2.1.5 L). In the literature, this technique has several names, all of which refer to the same underlying principle but different methods for collecting the data. Automated Diffraction Tomography [51], Electron Diffraction Tomography, Rotation Electron Diffraction, and Continuous Rotation Electron Diffraction, and Micro Electron Diffraction [16] are such examples.

A tilt series is important to structure determination in both 3D-ED and XRD. However, there are differences in the Ewald sphere between the two techniques. X-rays have longer wavelengths so the curvature of the Ewald sphere (the radius of which is reciprocally related to wavelength) is much greater than in ED. In ED, the Ewald sphere is much flatter, resulting in diffraction patterns which can lack 3-dimensional information. Therefore, tilting is crucial to structure determination. However, tilting a crystal whilst acquiring diffraction patterns may require significant dose and could destroy particularly beam-sensitive compounds before a full tilt series can be obtained from the crystal of interest: a problem for which SerialED (discussed in Section 2.1.5) aims to overcome.

Data Collection Protocols in 3D-ED

The standard available range of tilt angles is $\pm 60^\circ$. Often, tilt is hindered by physical problems in the TEM, such as the sample holder or grid getting in the way or by unwanted sample movement. This missing angular range, shown shaded in pink in Figure 2.4 R, is called the missing wedge although this is less of a problem than in tomography as smaller tilt ranges may be sufficient to solve structures with higher symmetry. Figure 2.4 R illustrates several different data collection protocols in 3D-ED. Acquiring discrete tilt series leads to imprecise integration between adjacent positions. Precession (Figure 2.4 B) can be used to mitigate this effect. Figure 2.4 C shows another approach: known as Rotation Electron Diffraction (RED). Here, a complete dataset is taken by using fine beam tilt steps for several different larger mechanical tilts. Finally, as pictured in Figure 2.4 D, continuous data collection also allows for the missing angles between adjacent tilt steps to be directly sampled. This reduces data collection times to less than a few minutes whilst managing to better sample reciprocal space [107]. The diffraction data here is collected as a movie. Whilst the crystal is continuously rotated, the detector is used in rolling shutter mode with a frame rate of ca. 4 s per frame [71].

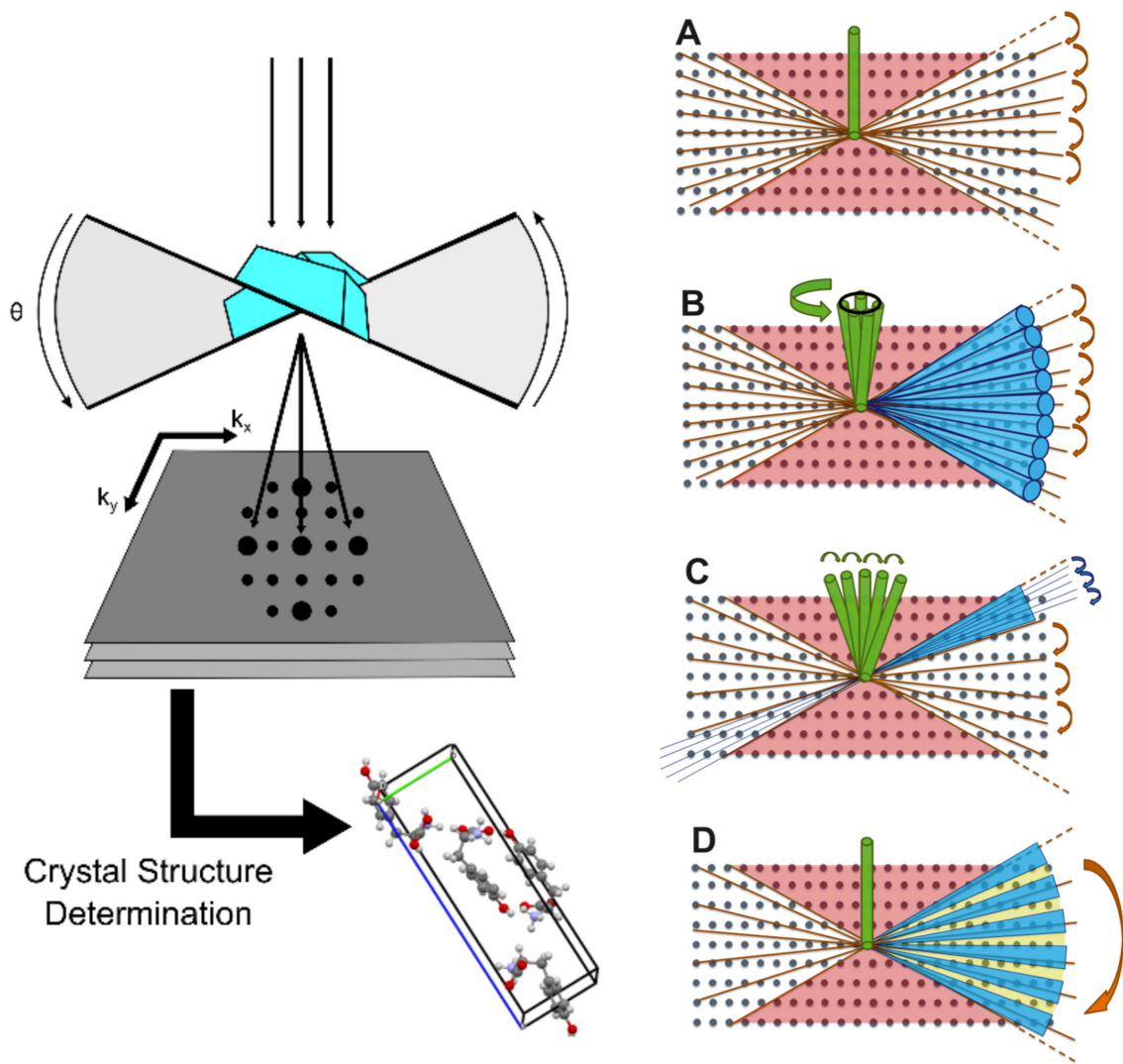


Fig. 2.4 Left: Schematic of using 3D-ED for crystal structure determination. Right: Different protocols for data acquisition in 3D-ED. A: stepwise acquisition B: step-wise acquisition with precession, C: Rotation Electron Diffraction, D: Continuous rotation acquisition. Right figure reproduced from [29].

2.1.5 Serial Electron Diffraction

Serial electron diffraction (SerialED) is a mix of both 3D-ED and SED. Instead of tilting one given crystallite to create a tilt series, the beam is scanned across the sample to collect one diffraction pattern each from many crystallites, analogous to single particle imaging in cryoEM. These patterns are combined to form a dataset which contains a range of tilts for the purpose of structure determination, as shown in Figure 2.5. However, this is susceptible to any preferred orientations of the crystals which would limit the sampling of reciprocal space in the combined dataset. This minimises the dose on each crystal required to collect a tilt series.

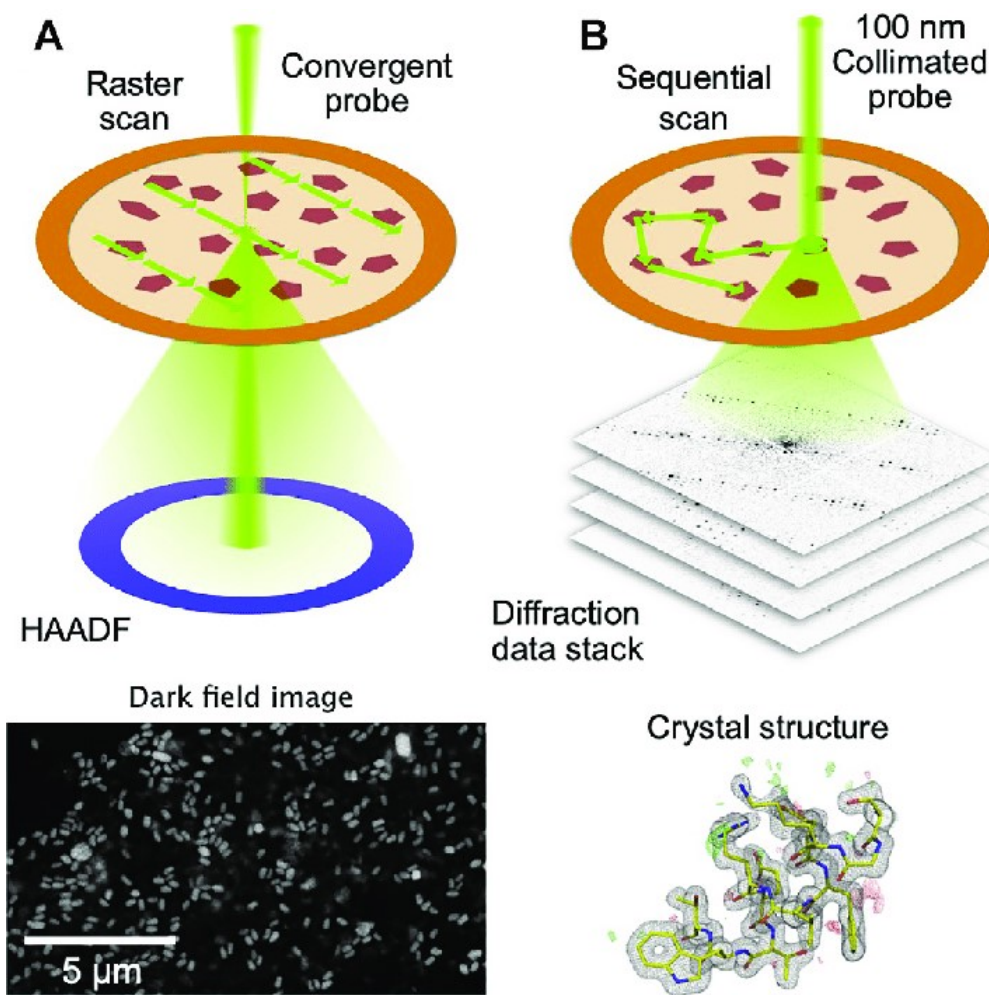


Fig. 2.5 Figure illustrating SerialED. In A), a low-resolution STEM image is acquired to locate potential crystals of interest. B) The beam is then steered to each crystal, collecting one diffraction pattern from each. This then forms a dataset which contains a range of tilts. Figure reproduced from [5].

2.2 Key Challenges of Electron Diffraction

Whilst ED presents a promising alternative to techniques such as XRD and NMR, there are particular challenges which are summarised below.

2.2.1 Kinematical vs Dynamical Diffraction

Electrons interact with a sample by elastically or inelastically scattering. Inelastic scattering signal is used for techniques such as EELS (electron energy loss spectroscopy), whilst elastically scattered electrons are useful for diffraction studies.

The scattered electron wave for a finite crystal can be obtained by summing over individual scattering amplitudes and is described as:

$$\psi_g = \sum_n F_g e^{-2\pi i \mathbf{s} \cdot \mathbf{r}_n} \quad (2.3)$$

where \mathbf{s} is the excitation error, and \mathbf{r}_n is the lattice vector of a given atom in the unit cell. \mathbf{r}_n is expressed as:

$$\mathbf{r}_n = n_1 \mathbf{a} + n_2 \mathbf{b} + n_3 \mathbf{c} \quad (2.4)$$

where n_1, n_2, n_3 are integers and $\mathbf{a}, \mathbf{b}, \mathbf{c}$ are lattice vectors. The excitation error \mathbf{s} is a measure of how a given reflection has deviated from the exact Bragg condition. The amplitude of a scattered wave can be modelled by the structure factor, F_g which takes into account the scattering due to a crystalline arrangement of atoms in a unit cell. It is defined in terms of the sum of all the individual atomic scattering factors of the atoms present in the unit cell [109]. The structure factor is written as:

$$F_g = \sum_i f_i e^{2\pi i (hx_i + ky_i + lz_i)} \quad (2.5)$$

where θ is the scattering angle, f_i is the individual scattering factor of i atom at position x_i, y_i, z_i in the unit cell, hkl are the Miller indices of the atomic planes from which the electrons were scattered, and \mathbf{g} is the scattering vector which is defined as:

$$\mathbf{g} = h \mathbf{a}_1^* + k \mathbf{a}_2^* + l \mathbf{a}_3^* \quad (2.6)$$

where \mathbf{a}_1^* , \mathbf{a}_2^* , and \mathbf{a}_3^* are reciprocal lattice vectors. Under 2-beam kinematical diffraction theory, it is assumed that an elastic scattering event only happens once within the sample before the electron is

transmitted and that only one diffracted beam is present. By assuming a perfect and finite crystal and integrating over the thickness, the intensity of the Bragg reflection is given by:

$$I_g(s, t) = \psi_g \psi_g^* = \frac{F_g^2}{k^2 V_c^2 \cos^2(\theta_B)} \frac{\sin^2(\pi ts)}{(\pi s)^2} \quad (2.7)$$

where t is the thickness, V_c is the volume of the unit cell, and θ_B is the Bragg angle. The constants in the equation can be grouped to define the extinction distance, ξ_g , which is a constant value for a given material and given scattering vector \mathbf{g} . It represents the thickness it takes for the scattered amplitude to become 0 such that there is an extinction of the reflection. It is a constant defined as:

$$\xi_g = \frac{\pi V_c \cos \theta_B}{\lambda F_g} \quad (2.8)$$

Equation 2.7 becomes:

$$I_g(s, t) = \left(\frac{\pi}{\xi_g} \right)^2 \frac{\sin^2 \pi ts}{(\pi s)^2} \quad (2.9)$$

which means that the intensity, I_g , is directly related to the square of the structure factor, F_g :

$$I_g \propto |F_g|^2, \quad (2.10)$$

However, this relationship does not make sense when $t > \frac{\xi_g}{\pi}$, as the intensity becomes greater than 1. To correct this, an approximation to 2 beam dynamical theory can be made, where the excitation error is now defined as:

$$s \rightarrow \sqrt{s^2 + \left(\frac{1}{\xi_g^2} \right)} \quad (2.11)$$

The intensities for 2-beam dynamical theory can now be modelled as:

$$I_g(s, t) = \left(\frac{\pi}{\xi_g} \right)^2 \frac{\sin^2 \pi t \sqrt{s^2 + \left(\frac{1}{\xi_g^2} \right)}}{\pi s^2 + \left(\frac{1}{\xi_g^2} \right)} \quad (2.12)$$

Dynamical theory accounts for multiple scattering events which give rise to the appearance of reflections forbidden under the kinematical approximation due to secondary scattering pathways, as illustrated in Figure 2.6.

In multiple beam theory, in which multiple diffraction conditions are considered, the intensities no longer simply vary proportionally to the structure factors. The intensities and presence of reflections are very sensitive to thickness, and exhibit a pendellösung effect. As a result, dynamical diffraction theory is

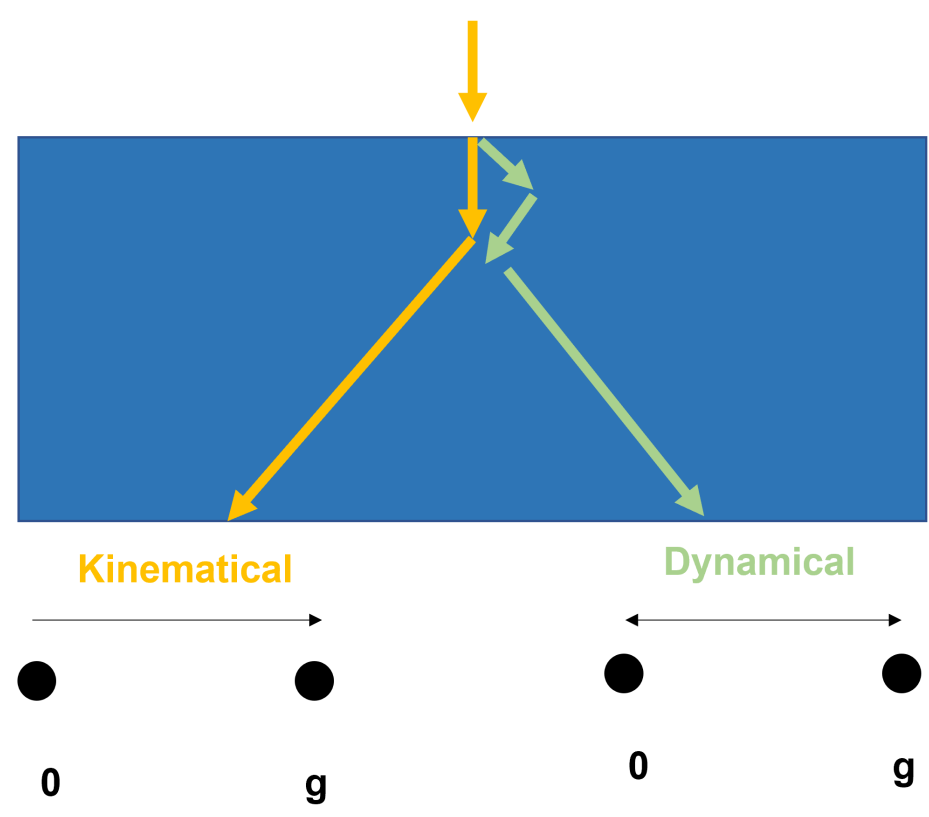


Fig. 2.6 Kinematical vs dynamical scattering under the 2 beam model. In dynamical scattering, scattering from the diffraction condition back to the central beam is also possible due to multiple scattering events.

required to accurately interpret scattering signals from electron diffraction, especially for thicker samples.

It should be noted that organic materials are relatively weak scatterers and there is substantial inelastic scattering which reduces the effects of dynamical diffraction. In proteins, scattering due to disordered surrounding bulk solvent also reduces dynamical effects further [55]. However, the importance of dynamical effects in organic molecules is contested within the community: with Sawaya et al. going so far as to state that the effects could be disregarded entirely [97]. The majority of crystal structures which have been refined from ED data have been done using kinematical approximations. This is because most methods currently used to analyse ED data have been adapted from XRD methods. XRD-based approaches only consider the kinematical theory of diffraction due to the weaker interaction that X-rays have with samples.

However, the implementation of dynamical diffraction theory is much more computationally expensive than kinematical theory. Alongside the difficult task of multi-parameter optimisation, this is the largest barrier to considering dynamical diffraction in the structure refinement process.

2.2.2 Large Unit Cells

Compared to inorganic materials, organic crystals have large unit cell parameters which presents intrinsically difficult problems in diffraction compared with smaller inorganic systems. In reciprocal space, a large unit cell translates to closely spaced diffraction spots which are difficult to resolve, especially in data which has a low signal to noise ratio due to beam sensitivity constraints [69]. In addition, a larger unit cell volume results in more diffraction spots appearing from different planes which meet the Bragg condition. As a result, the intensities of each spot are often further reduced as the signal is split across many reflections. These differences are illustrated in Figure 2.7, where the diffraction pattern of gold (metallic, face-centred-cubic) can be compared to the diffraction pattern of γ indomethacin (small organic molecule, triclinic). In addition, the atomic scattering factor will affect scattered intensities. The higher the scattering factor, the higher the scattering power. Organic materials have lower scattering factors which further result in lower intensities at each Bragg spot.

2.2.3 Beam-Sensitivity

Intermolecular forces such as van der Waals and hydrogen bonding hold individual small organic molecules together in their crystalline form. These forces are relatively weak and are therefore prone to destruction when exposed to electron irradiation. Whilst electron diffraction can be easily used to probe inorganic structures, low electron doses (ca. 1-100 electrons \AA^{-2}) must be used when probing APIs and acquisition

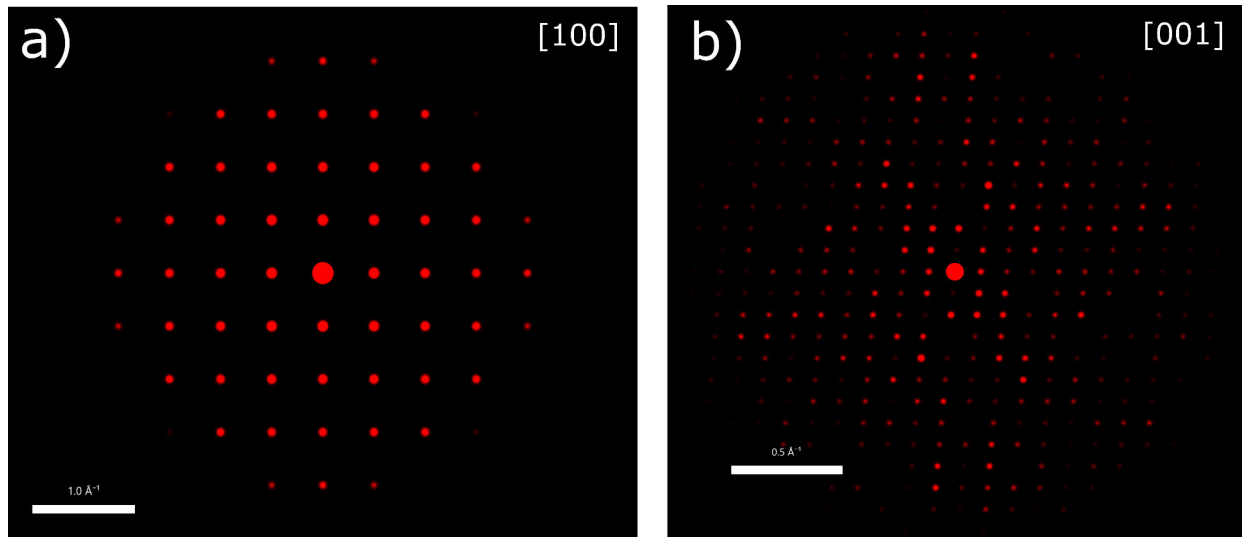


Fig. 2.7 a) the 001 diffraction pattern of a single crystal of gold, which has a lattice parameter of 4.08 \AA [74], b) the 001 diffraction pattern for a single crystal of γ indomethacin, the organic compound subject to investigation in Chapter 3, which has a lattice parameter of 9.23 \AA , 10.95 \AA , and 9.74 \AA and α of 69.4° , β of 110.8° , and γ of 92.8° . There are many more Bragg spots in b).

should be automated as much as possible. The beam sensitivity forces acquisition times to be kept short leading to a dataset with a low signal to noise ratio.

Beam Damage Mechanisms

Damage to the sample happens either due to elastically or inelastically scattered electrons. There are several main mechanisms for beam damage in a specimen [109]:

1. Radiolysis: inelastic scattering causes chemical bonds to break. This may result in a change of structure.
2. Sputtering: elastic scattering of an electron.
3. Heating: inelastic electron scattering causes a local increase in temperature which may lead to defect creation.

In organic materials, the primary damage is caused by inelastic scattering. This causes ionisation or molecular excitation which can result in the formation of free radicals, heating, or radiolysis. A consequence of these effects is the collapse of crystal structure. Whilst studied extensively in inorganic systems, knowledge about damage mechanisms in soft materials is limited. Cattle et al. observed that radiolysis in pharmaceutical materials led to a change in crystalline orientation, followed by loss of crystallinity [12], which was measured by recording electron diffraction pattern intensities. Intensities

of spots can fade as crystallinity is lost. This is because electron irradiation causes a local loss of order to individual crystal planes which gradually spreads until the damage is widespread. Spot intensities may also broaden or shift as a result of damage to individual molecules which distorts the lattice [88].

Damage can be reduced using several strategies. Firstly, using high-voltage electrons in the illuminating radiation reduces damage because of the reduction of energy dissipation within the sample with increasing high voltage [88]. Secondly, liquid nitrogen temperatures (cryo-EM) can be used to suppress secondary damage effects which require diffusion of reaction products.

2.3 Analysis of Electron Diffraction Data

3D-ED and SED data consists of a set of related diffraction patterns. If the quality of data is sufficient, Miller indices can be assigned to each reflection and each reflection's intensity is also recorded. Indexation provides information about the unit cell, and can reduce the number of possible space groups to a handful. In 3D-ED data, diffraction patterns are rotationally related, which makes indexation easier than when dealing with isolated diffraction patterns. These patterns can be used for structure solution. Diffraction patterns collected from SED are spatially related in 2-dimensional space. SED data is much harder to index and until recently, in the case of SerialED [100], has not been used for structure solution.

2.3.1 SED Data: Probing Microstructure

In SED data, one diffraction pattern is acquired for each pixel in a real space image. In this way, it is possible to probe a sample's microstructure: for example, identifying crystal defects using virtual imaging.

Virtual Dark Field Images

Given that an entire diffraction pattern is recorded for each pixel, virtual detectors of any shape or size can be constructed by integrating the relevant pixels in the pattern. As illustrated in Figure 2.8, by plotting the measured intensity as a function of probe position, virtual dark field (VDF) images may be formed and are powerful tools for observing crystallographic contrast. For each given dataset, multiple VDFs can be constructed to observe and compare different parts of the sample at different diffraction conditions. In work by Johnstone et al., VDFs were combined to form composite images which revealed small changes in orientation [40]. The use of SED for probing the microstructure of beam sensitive systems has also been demonstrated in metal-organic frameworks [40], perovskites [34], and cellulose [108].

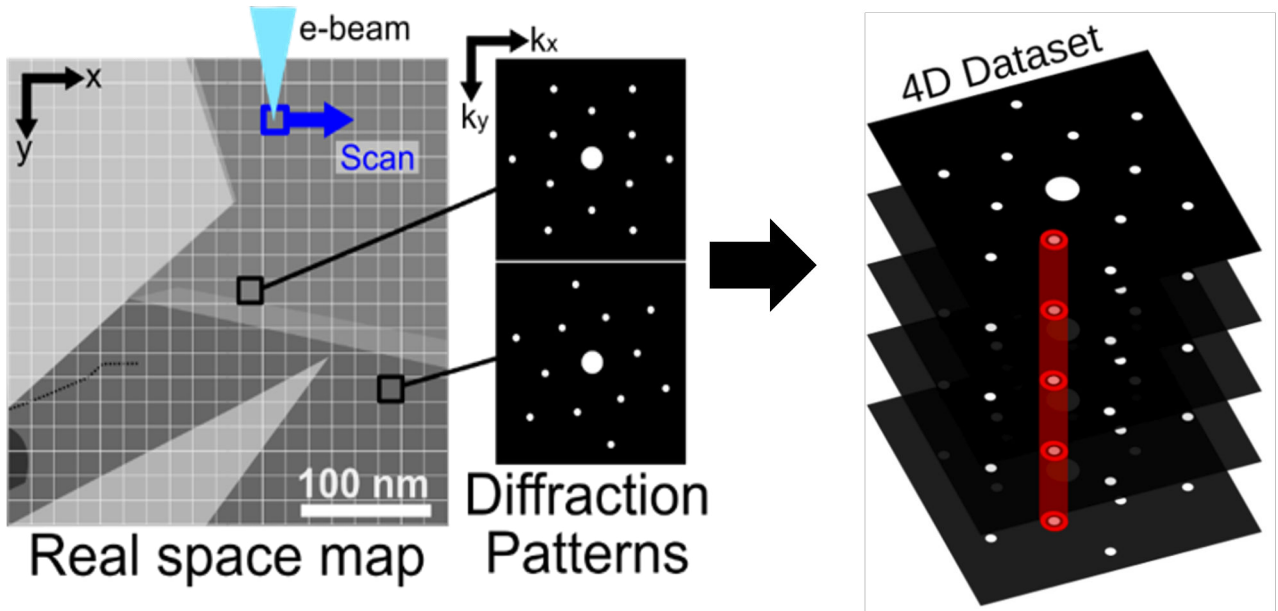


Fig. 2.8 The resulting 4D dataset from SED data can be used to create virtual apertures and virtual images by integrating the relevant pixels in the pattern.

2.3.2 3D-ED Data: Solving Crystal Structures

There are two main stages to extracting structural information from 3D-ED data: structure solution, and structure refinement. Before this, a process called integration is performed. This requires finding the peaks in each diffraction pattern collected (their measured intensities are not required at this stage). The peak positions are then used to find information about the unit cell of the system. There is software available which can be used for this first stage, namely: eADT [51], PETS2 [78], XDS [43], CrysAlis (commercial software), DIALS [16], and APEX4 (commercial software). Once this has been determined, structure solution and refinement can begin.

Structure Solution

After the basic unit cell has been identified, structure solution begins, with the aim of recovering the phase from measured electron densities. Under kinematical theory, measured intensities are related to the modulus square of the structure factor (a complex property). Phase information, which is required to compute the location of atoms within the unit cell directly through Fourier synthesis [102], is lost. This is known as the phase problem for which many methods have been developed to ‘recover phase’. In direct space methods, a trial structure is initially developed by varying a structural model around a unit cell: and comparing the structure’s diffraction pattern to the observed diffraction pattern. Other methods, such as direct [3] or Patterson methods [82], are most popular for small organic molecules whilst

molecular replacement [26] or experimental phasing [63] are most popular for use with macromolecules. The process of finding the best trial structure is analogous to finding a global minimum on a hyper-surface. There are several global optimisation methods available, namely simulated annealing by the Monte Carlo method [32] (used by Partha et al. for rameletoe [21]), or a genetic algorithm [45] (used by Smalley et al. for L-tyrosine [99]). The software available for this include: SHELXS/T/D [98], Superflip [79], SIR [3], XLENS [91]. Ab initio calculations such as AIRSS [86] and other DFT methods can also be used to suggest trial structures.

These methods provide a set of atomic coordinates to a reasonable accuracy. However, structure solutions are not reliable for precise atomic positions, detail of a structure, or even atomic types [11]. To improve this information, structure refinement is needed.

Structure Refinement

After structure solution, the structure factors and intensities calculated from the initial proposed structure do not exactly match with the experimentally measured values. This error is caused by approximations in structure solution methods, experimental errors, and errors in finding the maxima in Fourier synthesis (which determines electron density maps) [11]. Structure refinement is an iterative method which acts to minimise this discrepancy in structure factors, most commonly using a least-squares metric.

Refinement can be aided by the use of constraints and restraints. Constraints relate two parameters subject to refinement, which reduces the total number of independent parameters that need to be fixed. Examples include positional constraints, which are controlled by the geometries of the atoms based on known facts about the unit cell symmetry. Restraints are used to introduce information about a compound into the refinement process which are less well defined than constraints (e.g. bond lengths can be restrained to within a certain range). However, this can easily cause bias and wrong solutions, so caution should be used when applying restraints to prevent incorrect structure refinement.

The R-factor is a figure of merit to determine the success of a model and is a measure of agreement between calculated and observed intensities. Whilst high values are good indications of a poorly-refined structure, low R-factors are not necessarily indication of a very good structure as this may be dependent on the theoretical model used to compare observed intensities. For example, if a purely kinematical model is used, dynamical effects are ignored which might impact the optimisation. Depending on the experiment, different R-factor definitions may be quoted. For 3D-ED data, the R-factor, R_F , is defined as such:

$$R_F = 100 \times \left(\frac{\sum_i |F_{o,i} - F_{c,i}|}{\sum_i |F_{o,i}|} \right) \quad (2.13)$$

where $F_{o,i}$ are the observed amplitudes, $F_{c,i}$ are the calculated amplitudes.

In general, there are several ways in which structure refinement (for electron diffraction data) can be approached. Firstly, it is possible to simply ignore any dynamical effects and do a fully kinematical refinement. Secondly, it is possible to correct the data approximately using extinction corrections or statistical dynamical corrections, where the weak intensities are corrected to suppress their increase. Thirdly, it is possible to measure integrated intensities, by either precessing the beam or by doing continuous rotation data acquisition, as shown in Figure 2.4. The difference in their respective effects is not well documented but it is agreed that both methods help to make the intensities ‘more kinematical’. The final method requires the most computational time but is the most accurate, which is to fully take into account dynamical effects by undertaking dynamical refinement. In this method, the thickness of the crystal must be refined, and the reflections are chosen based on their proximity to the Ewald sphere. Whilst kinematical calculations take a matter of seconds, dynamical calculations may take several hours. Full dynamical refinement is possible for small organic molecules but calculations would take too long to dynamically refine a protein’s structure in practice. Therefore, alternative routes such as rank refinement [24] could offer an alternative approach. The relative success of these methods may be evaluated by comparing the resultant R-factors.

The acceptable R-factor value varies depending on the structure being solved. In 2015, 94% of the crystals in the Cambridge Structural Database of small-molecule structures had R-factors less than 10% [30]. However, R-factors are generally much higher for macromolecules and a value of 10% would be considered excellent. There is also a noticeable difference (illustrated in Figure 2.9) between R-factors from structures which have been kinematically vs dynamically refined which points to the necessity to use dynamical refinement and possibly precession to improve R-factors.

There are many refinement software packages available for use with electron diffraction data, the majority having been adapted from XRD methods. Such examples are SHELXL [98], PHENIX [1], and DIALS [16]. Palatinus et al. have developed software (PETS, JANA) [78] to incorporate dynamical diffraction into data analysis of ED.

Structures Solved Using 3D-ED

The use of 3D-ED to solve both organic and inorganic structures has recently become increasingly routine. Some main case studies of small organic molecules have been summarised in Table 2.1. The majority of these structures have been solved without the use of any dynamical refinement and have already been solved using XRD. The next step would be to demonstrate the use of ED in solving structures where

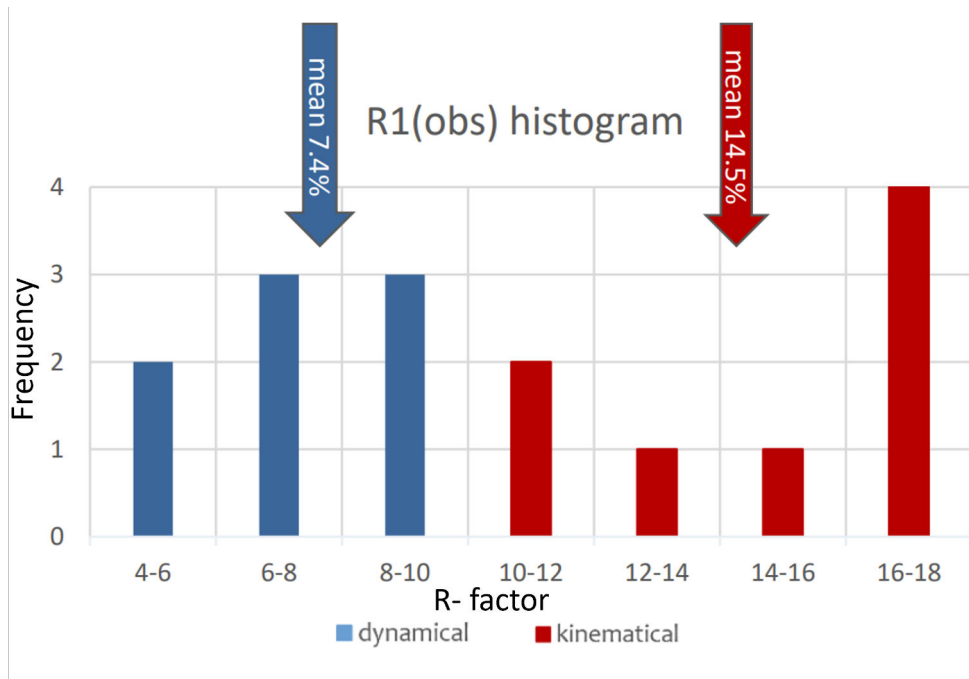


Fig. 2.9 The mean R-factor from 8 structures when dynamically refined is lower than the R-factors resulting from their kinematical refinement [76].

XRD has proved unsuccessful.

Size of Typical Active Pharmaceutical Ingredients

Whilst 3D-ED has been extensively developed for accurate structure determination, the structures solved remain comparatively small in size. To our knowledge, the largest small organic molecular structure solved by 3D-ED to date is a co-crystal of sofosbuvir and L-proline with a combined molecular weight of 644 gmol^{-1} [9]. It should be noted that Nannenga et al. have managed to used ED to solve the structures for much larger macromolecules such as catalase, albeit without any dynamical consideration. The structure of catalase was determined with an R-factor of 26% [71]. Despite this high R-factor value, this work demonstrates that the technique is not limited to small organic molecules.

In comparison to small organic molecules solved with 3D-ED (the small organic molecules in Table 2.1 have an average molecular weight of 341 gmol^{-1}), the molecular weight of new small organic molecules approved by the FDA in 2020 is larger with an average molecular mass of 492 gmol^{-1} [68]. Electron diffraction techniques need to be further developed for routine structure determination of larger small organic molecules to suit the pharmaceutical industry's needs. Traditionally, small organic molecules have not tended to be developed much larger than 500 gmol^{-1} due to Lipinski's rule of five, which states that oral availability of compounds decreases as molecular weight reaches a critical value [58]. However,

Small Organic Molecule	Workflow	R-Factor (%)	Size of molecule (g/mol)	Sample Preparation
Paracetamol [77]	Precession + Dynamical Refinement	10	151.2	Crushed powder directly deposited onto holey-carbon Cu TEM grid
Orthocetamol* [35]	Precession + Kinematical Refinement	37	151.2	Crystallised platelets were crushed and loaded onto carbon-coated Cu TEM grid
L-tyrosine [99]	Kinematical Refinement	41	181.2	Dry powder of L-tyrosine was deposited onto continuous carbon film (supported by Cu grid)
Co-crystal: Sofobusvir/L-proline* [9]	Precession + Dynamical Refinement	12	644	Co-crystals were fished from oversaturated ethanol solution onto carbon-coated Cu TEM grids
Cabotegravir [38]	Continuous RED	n/a	405.4	As milled nanopowder deposited onto carbon coated TEM grids
Ramelteon [21]	Precession	24	269.3	Crush dry crystals into a fine powder between two glass plates, then sprinkle on holey carbon TEM grid
Loratadine [111]	Precession + Kinematical Refinement	25	382.9	Crush dry crystals between two glass slides, then sprinkle on holey carbon TEM grid
δ indomethacin* [57]	ContinuousRED + Kinematical Refinement	19	357.8	Crush dry crystals, then gently load on holey carbon TEM grid

Table 2.1 Table to show notable studies where 3D-ED was used for structure solution and refinement. '*' indicates structures which had not previously been solved using XRD.

the pharmaceutical industry is moving away from focussing on oral solid dosage methods (although smaller molecules which follow Lipinski's rule still dominate the market), and there is increasing focus on delivery mechanisms which will move away from the rule of five. For example, in long-acting injectables, large molecular size is instead used as an advantage in order to manipulate low solubility for use in slow-release medicines.

2.3.3 TEM Sample Preparation

All samples used for ED must be electron transparent, meaning samples should be no thicker than around 100 nm. There are several methods by which pharmaceutical samples can be prepared for ED, depending on what is being studied. Methods for 3D-ED sample preparation is relatively simple: crushed powder is directly deposited onto a holey-carbon Cu TEM grid as shown in Table 2.1. However, different sample preparation methods may be required for tasks other than structure solution. For example, a study on a tablet cross-section might require field-ion beam milling and microtoming to curate a thin slice of the tablet without altering its microstructure. This would give insight into potential aggregates, particle size distribution and therefore likely macroscopic properties of the tablet.

Chapter 3

Amorphous Solid Dispersions

Amorphous solid dispersions (ASDs) are a formulation strategy used to overcome the poor solubility of active pharmaceutical ingredients (APIs). In this chapter, the effect of varying API to polymer ratios in an indomethacin - polyvinylpyrrolidone (PVP) ASD is investigated using scanning electron diffraction (SED) and X-ray powder diffraction (PXRD).

3.1 Literature Review

Low aqueous solubility of an API can be a problem to the pharmaceutical industry. In 2010, 40% of marketed drugs and 90% of drugs in development had poor aqueous solubility [60] which reduces their bio-availability in oral dosage forms. To overcome this, a popular approach is the use of ASDs. The API is blended with an amorphous water-soluble excipient to create a solid dispersion with improved solubility. Other alternatives to this method include the use of co-crystals and self-emulsifying formulations [103].

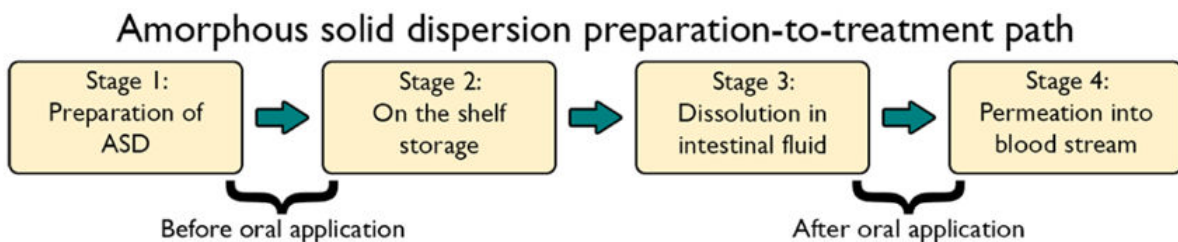


Fig. 3.1 Before their oral application, ASDs may have a limited shelf-life due to unwanted crystallinity which may be residual from Stage 1, or develop during Stage 2 [90]. This will affect their performance in Stages 3 and 4.

The biggest challenge for ASDs is unwanted crystallinity due to the metastable nature of the amorphous API which can limit their shelf-life, as shown in Figure 3.1. This crystallinity is dependent on manufacturing methods and storage conditions of the drug [15]. The presence of excessive crystallinity requires careful control because it reduces the solubility of the API which can affect drug efficacy. In industry the crystallinity is currently tracked using bulk characterisation techniques at the quality control stage of ASD manufacturing. PXRD, which has a limit of detection on the order of 1-5%, is used to assess the quality of ASDs in industrial quantities. Other techniques can assess a sample at both the molecular and bulk level. They include; differential scanning calorimetry (DSC), solid state nuclear magnetic resonance (SSNMR), Fourier-transform infrared spectroscopy (FTIR), electron energy loss spectroscopy (EELS) [20], and polarised light microscopy (PLM) [15]. However, the use of these techniques for probing nanoscale crystallinity is limited and an in-depth understanding about the distribution and nature of any crystallinity on the nanoscale is generally less well understood. Instead, electron diffraction is an ideal candidate for this task. As shown by S'ari et al., TEM is a valuable way to find distinct areas of crystallinity. In their work using selected area electron diffraction (SAED), polymorphs of felodipine within a felodipine - PVP ASD could be identified [96]. Moseson et al. were similarly able to show the ability of TEM to detect crystallinity in a hot-melt extruded ASD which appeared amorphous using XRD and DSC [67]. However, with such beam sensitive samples, investigations are limited by the time that a region of sample can be illuminated for before the features being observed are destroyed. This significantly limits conventional TEM techniques. In contrast, SED is a technique which holds promise for exploring and quantifying crystallinity on the nanoscale whilst working around this problem. By collecting data at each pixel, virtual apertures can be reconstructed after data acquisition to highlight areas of crystallinity using methods described in Section 2.3.1. To our knowledge, no investigations into ASDs using SED exist in the current literature.

3.1.1 Factors Affecting Crystallinity in ASDs

Phase separation and eventual resulting crystallinity (as illustrated in Figure 3.2) is dependent on the glass transition temperature T_g of the system. This is affected by various factors:

1. Raising the temperature at which ASDs are stored will reduce their shelf-life due to higher molecular mobilities closer to T_g which accelerates the phase separation process.
2. Decreasing the polymer concentration will lower the T_g of the ASD. The addition of the amorphous polymer is used to raise the T_g of the system. The amorphous polymer is chosen such that hydrogen bonds can form between the API and polymer which raise the kinetic stability of the ASD [8].

3. The presence of water or humidity will further depresses the glass transition temperature by causing a plasticising effect [27]. In addition, any absorbed water could compete with the hydrogen bonds formed between the hydrophilic polymer and API which are important to elevating the T_g of the system [112].

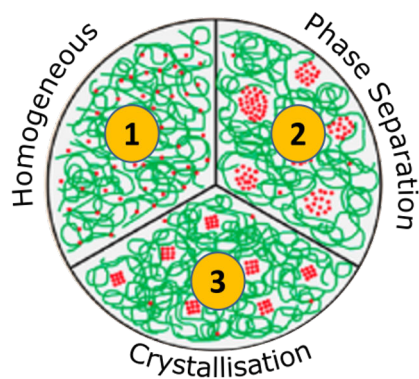


Fig. 3.2 Green represents the amorphous water-soluble polymer excipient. Red represents the API. (1) indicates the desirable form of the ASD. However phase separation (2), may lead to eventual crystallisation of the API (3), which reduces dissolution rates. Adapted from Ricarte et al. [89].

3.1.2 Manufacturing Methods for ASD Synthesis

There are many ways to create a solid dispersion, as shown in Figure 3.3. The ways in which the ASD is formulated will affect its characteristics. In industry, hot melt extrusion is used to produce ASDs en masse. This involves processing constituent components above their T_g in order to create effective molecular level mixing. Twin screws mechanically grind the ASD during production which can introduce deformation-induced molecular mobility in the final product. In contrast, rotary evaporation (a subset of the solvent evaporation method) is commonly used on the smaller scale and doesn't necessarily require the heating of any constituent components.

3.1.3 Indomethacin - PVP: a continuation of a previous study within the group

A proof-of-principle investigation using SED on an indomethacin-PVP system had already been carried out within the group prior to this project. Indomethacin is a small organic molecule used as an anti-inflammatory drug. It was chosen as an API due to its ease of availability and it is a relatively well-studied system. In addition, the existence of chlorine in its molecular structure allowed for the

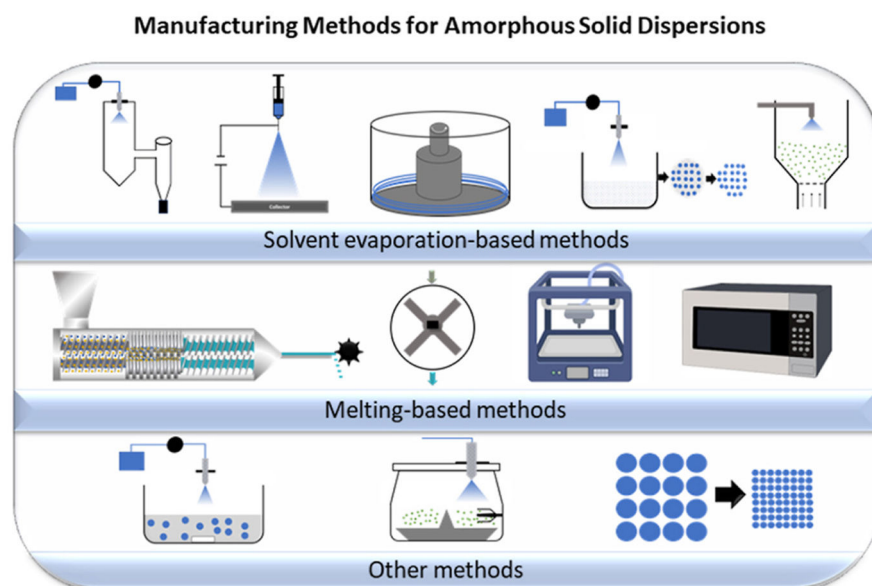


Fig. 3.3 Illustration of the two main manufacturing methods for ASDs; melting-based or solvent evaporation-based methods. Figure reproduced from Bhujpal et al. [8].

possibility of using energy dispersive X-ray spectroscopy (EDX) to confirm any results. Indomethacin has several polymorphs, as shown in Figure 3.4 b).

ASDs were synthesised using a solvent evaporation-based method in a vacuum furnace at ca. 50 - 80 °C. Data was collected by Duncan Johnstone at ePSIC¹ and analysed by Matthew von Lany. Their reported findings show that crystallinity could be detected using ED below the limit of PXRD (Figure 3.5), which is consistent with Moseson et al. [67]. In addition, the acquisition conditions were shown to preserve the structure of the nanoparticles such that interpretable contrast could be extracted. Crystalline nanoparticles of indomethacin were indexed to the γ polymorph, as shown in Figure 3.6. Finally, an apparent solubility limit for indomethacin within PVP was placed between 30 - 70 wt%. These conditions were used as a benchmark for the subsequent investigation presented in this chapter. Some of this data was re-analysed to aid the progress of the new investigation.

In addition to findings from Johnstone and von Lany, the apparent solubility limit of indomethacin in PVP has been documented in the literature although with conflicting answers depending on manufacturing methods. Knopp et al. record a solubility of 38-40 wt% indomethacin in PVP [50]. However, Yoshioka et al. find that samples made up to 90 wt% were amorphous under XRD (these samples were made using rotary evaporation methods)[113]. Mohapatra et al. showed similar results, finding

¹electron Physical Sciences Imaging Center, based in Oxfordshire, UK

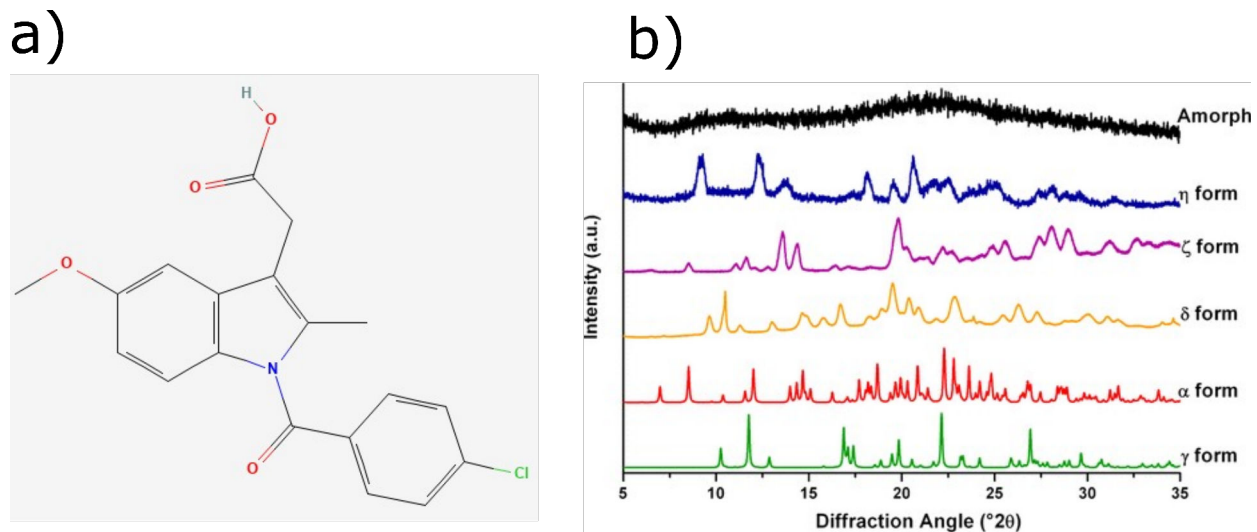


Fig. 3.4 a) The indomethacin molecule. The chlorine allows for the possibility of using EDX. b) XRD traces of known polymorphs of indomethacin. Due to difficulty in isolating polymorphs, only the crystal structures of α , γ , and δ are known. Figure reproduced from [101].

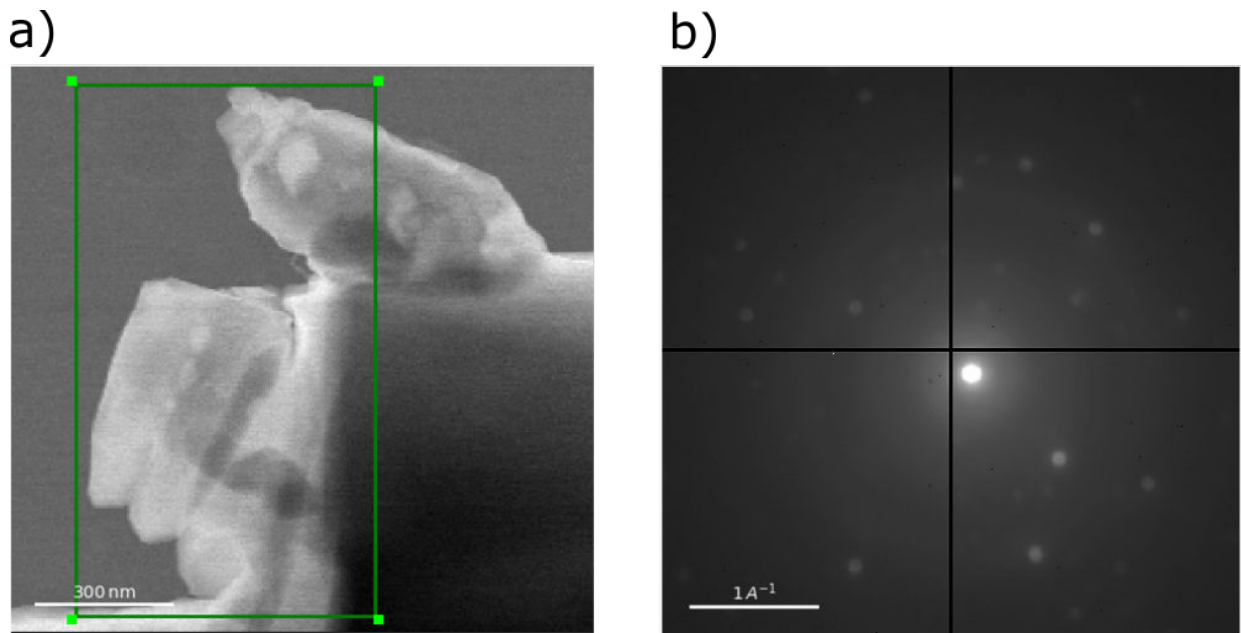


Fig. 3.5 Samples which appeared amorphous in XRD had areas of nanocrystallinity as can be seen by the presence of sparse Bragg spots. a) a cluster of nanoparticles of ASD. b) the summed diffraction pattern from the area highlighted in a) indicates the presence of crystallinity. There are multiple crystallites within the summed area leading to Bragg spots corresponding to different crystallites. Data taken by Duncan Johnstone on JEOL ARM 300F microscope operated at 300 kV with a convergence semi-angle of 0.6 mrad. The beam current was 2 pA.

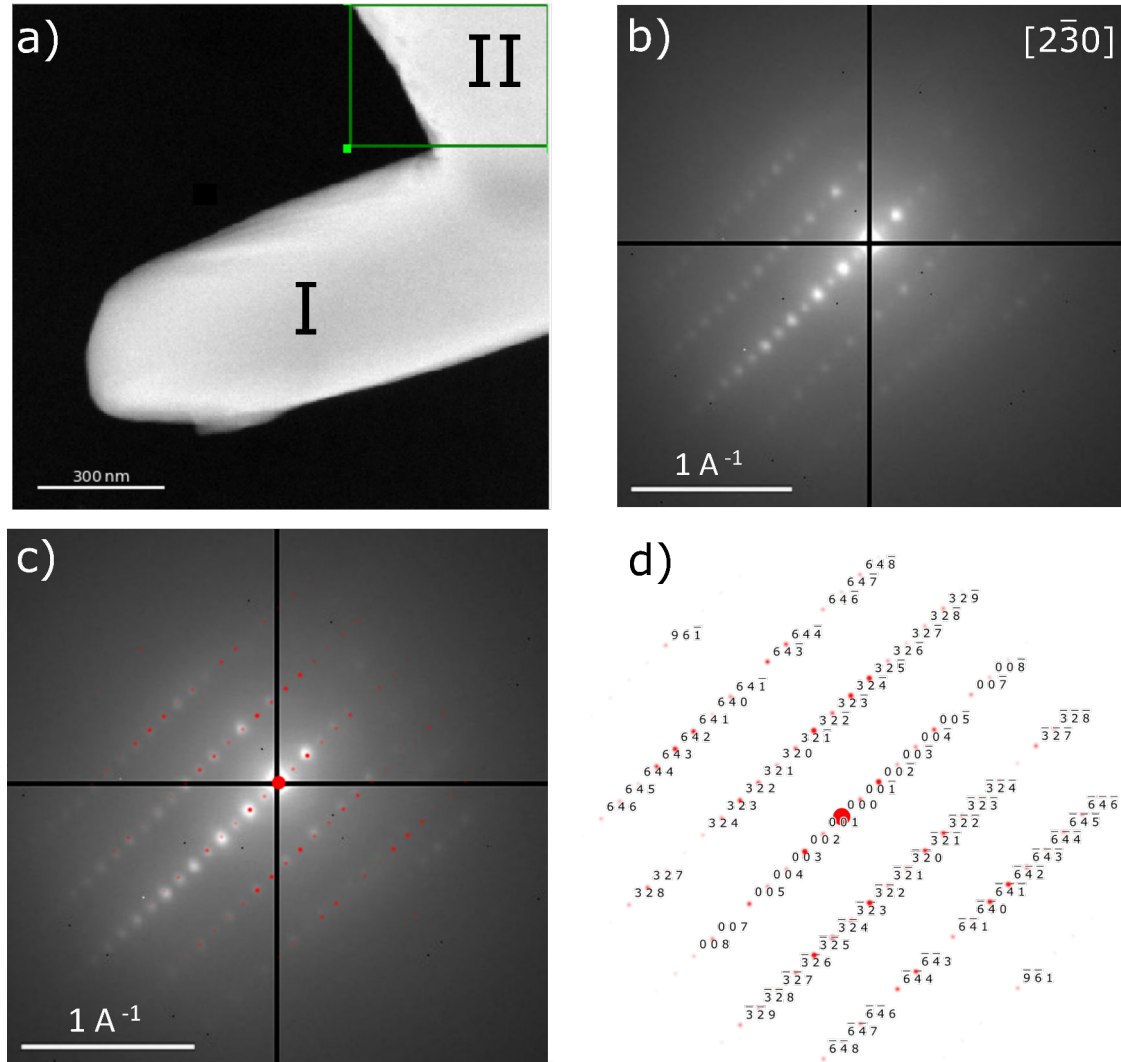


Fig. 3.6 Indexing the indomethacin particle (a, II) from 70 wt%. b) The long d-spacing allows for unambiguous indexing to the γ polymorph. c) The fit to the indexing. d) The diffraction pattern with labelled reflections. The summed diffraction pattern in b) indicates only one crystallite present in region II. The other particle (a, I) was crystalline but there were not sufficient Bragg spots observed to be able to index it. Data taken by Duncan Johnstone with the same conditions as in Figure 3.5.

crystallinity in ASDs of indomethacin at 85wt% [66] which is in line with findings by Crowley et al. [19].

This ambiguity over the solubility limit led to the motivation to systematically study the limit across a wider range of ASD compositions. Based on the review of the literature, the aims of this investigation were to:

1. Establish a solubility limit to compare results to the varying values suggested in the literature
2. Explore the microstructure of semi-crystalline solid dispersions
3. Confirm the presence of any polymorphs of indomethacin within local areas of the sample
4. Explore the limit of detection of crystallinity in PXRD compared to SED

3.2 Method

3.2.1 Experimental Methods

ASD Synthesis

The experimental methods used for ASD synthesis aimed to closely follow the solvent evaporation method described by Pham et al. [85]. The appropriate weight % compositions of indomethacin and PVP were made up such that the total mass of the combined powders was 0.5 g. The powder was then dissolved in approximately 60 cm³ of dichloromethane to form a yellow solution. This was placed into a sonicator for 10 seconds to ensure full dissolution. A rotary evaporator was used to boil off the solvent which was placed in a water bath at 40 °C under a pressure of 50 - 100 mBar. Whilst indomethacin and PVP are more soluble in ethanol and this was a suggested solvent used by Pham [85], lack of volatility of the ethanol caused a sticky viscous film to form during rotary evaporation from which a powder could not be obtained. Samples were made at 20 wt%, 30 wt%, 40 wt%, 50 wt%, 60 wt%, 70 wt%, 85 wt%, and 95 wt% indomethacin - PVP. For samples between 20 wt% and 70 wt%, the dichloromethane solution foamed at the final stages of solvent evaporation, forming a brittle glassy foam. For the 85 wt% and 95 wt% samples, a chalky pale yellow powder was formed instead. In each case, the product was broken up gently in a glass vial and put into a dynamic vacuum at room temperature overnight to allow remaining solvent to evaporate. The resulting large, dry particles were then crushed for around 1 minute with an agate pestle and mortar to create a fine powder.

beam-induced damage?

TEM Specimen Preparation

Holey carbon 3 mm copper discs were shaken in the fine powder to directly deposit the sample onto the TEM grids. These were stored in a dessicator upon assembly until use.

SED Data Acquisition

SED data were acquired using a Spectra 300 microscope operating at 300 kV. Dwell time was 1 ms per probe position, with scan areas of ca. 1 micron. One 4D-SED dataset was acquired in around 1 minute. The beam current was measured using a Faraday cup to be 2.3 pA with a convergence angle of 0.6 mrad giving a diffraction-limited probe diameter of ca. 4 nm.

A Merlin Medipix detector recorded 256 x 256 diffraction patterns. It was operated in single pixel mode with a threshold voltage of 50 kV. Particles on the carbon grid which were thin enough to be electron transparent were chosen manually by observing live images on the HAADF detector. Care was taken to blank the beam immediately before and after SED data acquisition to minimise beam damage. No particle was scanned more than once.

Calculating Dose from Experimental Conditions

The Spectra microscope is equipped with a Faraday cup which enables the current to be measured accurately. In this way, the electron dose can be calculated assuming a disc-like probe. From the current, the number of electrons per second can be calculated. Next, the number of electrons (arriving at each pixel) is calculated using the dwell time. The dose is found by dividing this by the area of the electron probe. This is true for the case that the probe size is smaller than the step size.

With a beam current of 2.3 pA, convergence angle of 0.6 mrad, dwell time of 1 ms, and accelerating voltage of 300 kV:

$$\text{Number of electrons in the probe} = \frac{2.3 \times 10^{12} \text{ C s}^{-1}}{1.6 \times 10^{-19} \text{ C electron}^{-1}} = 1.25 \times 10^7 \text{ electrons} \quad (3.1)$$

The number of electrons on one pixel is:

$$1.25 \times 10^7 \text{ electrons s}^{-1} \times 10^{-3} \text{ s} = 1.25 \times 10^4 \text{ electrons pixel}^{-1} \quad (3.2)$$

With a convergence angle of 0.6 mrad, the probe is diffraction limited. Therefore the radius of the probe is given by:

$$r = \frac{0.61 \lambda}{\sin \alpha} \quad (3.3)$$

where $\alpha = 0.6 \times 10^{-3}$ rad, $\lambda = 1.97$ pm for an accelerating voltage of 300 kV. The radius of the probe is therefore 2 nm, giving an area of 1260 \AA^2 . The dose is:

$$\text{Dose} = \frac{1.25 \times 10^4 \text{ electrons}}{1260 \text{ \AA}^{-2}} \quad (3.4)$$

giving a dose of ca. 10 e \AA^{-2} . In practice, the beam area will be larger than the theoretical value calculated. Therefore, this is an upper bound for dose.

EDX Data Acquisition

Immediately after SED, an EDX map was acquired in order to confirm the identity of the particle and identify possible contamination. Instead of changing apertures, the monochromator was used to increase the beam current 100 times to around 200 pA in order to generate sufficient signal for EDX mapping. A scan speed of $1 \mu\text{s}$ was used. Acquisition was stopped once enough scans were completed to provide a clear signal with no obvious contaminants, typically taking around 2 minutes.

Powder X-ray Diffraction

A Bruker D8 DAVINCI machine was used to acquire powder X-ray diffraction data. In accordance with the methods used in Pham et al. [85], a step size of 0.0167° was used, with a continuous 2θ scan range of 2° to 60° . A continuous rotation of the stage was set to 25 rpm. All the reflections of interest were within this range given the large unit cell size of indomethacin. Intensities were then corrected to fixed divergent slits using commercial EVA software.

Differential Scanning Calorimetry

Differential scanning calorimetry (DSC) is a bulk method which indicates whether a sample has a sharp glass transition temperature, T_g and therefore whether or not it is crystalline. The Q2000 machine was used to perform DSC. Samples were heated under a nitrogen atmosphere on an aluminium pan at a heating rate of $10^\circ\text{C}/\text{min}$ over the temperature range of $5 - 300^\circ\text{C}$.

3.2.2 Data Processing

Pyxem was used to align, center, and calibrate the SED data [39]. Both CrystalMaker and Pyxem were used to index individual diffraction patterns. These methods are described below.

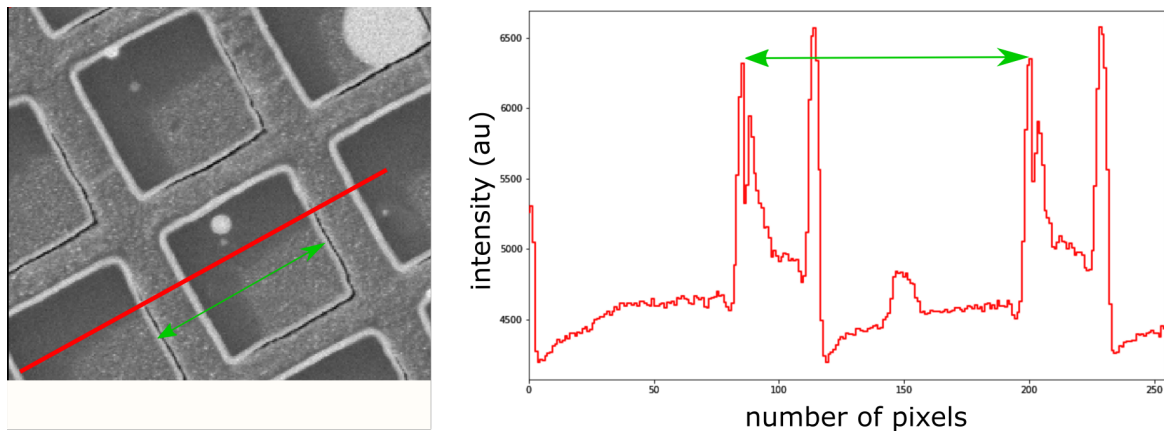


Fig. 3.7 Calibrating real space values using a diffraction cross grating. A line trace is used to measure the spacings accurately.

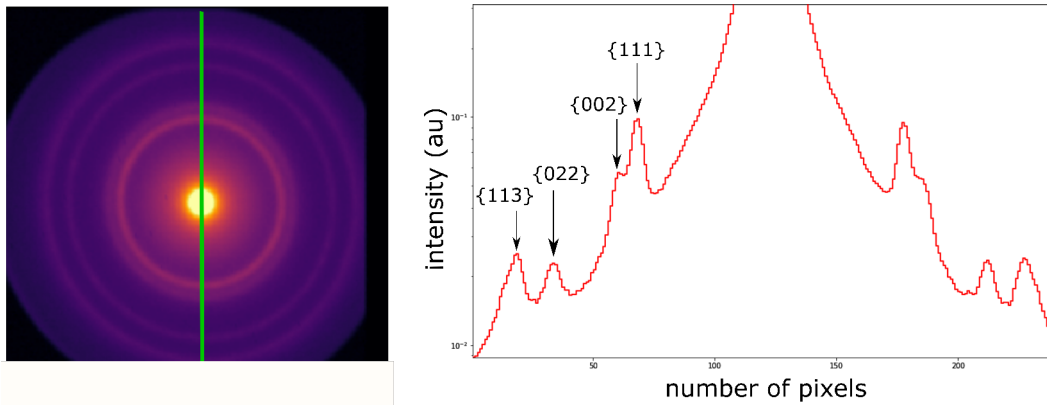


Fig. 3.8 Polycrystalline Gold Diffraction Pattern used to retrieve alignments for a given camera length. A line trace is used to measure the spacings accurately.

Calibrating and Centering Data

Calibration was done using an agar scientific Palladium Gold cross grating. The calibration routine followed had been developed within the group and was not altered significantly for this work. For calibration of real space, the cross grating specifications provided by the manufacturer were 2160 gratings per mm. Therefore, the spacing between each grid is 463 nm. This was used to find the number of nm represented by each pixel in the SED images at a given magnification, as shown in Figure 3.7. For calibration of reciprocal space, the polycrystalline diffraction pattern of gold was used. Given that the lattice spacing of gold is 4.08 Å, the d_{hkl} distances can be calculated and compared for a given camera length, as shown in Figure 3.8.

Centering algorithms available in Pyxem were used to center each diffraction pattern [39]. Out of the three available methods, the cross-correlation method was used. Circular elements of multiple sizes

within a range set by the user are cross-correlated. The maximum of the cross-correlation determines the center of the direct beam and this position is shifted to the center of the data array [37].

Indexing individual diffraction patterns

Diffraction patterns were summed over areas which appeared to be a single crystallite to form a pattern with a high enough signal to noise ratio to potentially be indexed. Extreme caution was required in this step due to the nano-crystalline nature of the samples with crystals of multiple orientations. In addition, the polymorphic nature of the samples meant that several possible structures could be present. Indexing of these diffraction patterns was done using the following steps.

Firstly, the characteristic d -spacings of the diffraction pattern were measured, giving $d_{1,hkl}^*$ and $d_{2,hkl}^*$. For each possible candidate structure, the list of reflections was sorted by intensity. Then, possible planes corresponding to the reciprocal spacings were selected. CrystalMaker was used to find an crystallite orientation and a simulated diffraction pattern was created. The geometries of the simulated and observed diffraction patterns were compared to see if there was a good fit. If not, the process was iterated. Some particles are easier to index than others, which occurs when characteristic short $d_{1,hkl}^*$ spacings appear. At large plane spacings, there are fewer possible miller index planes resulting in lower ambiguity here. Once the first family of reflections could be assigned, the planes corresponding to $d_{2,hkl}^*$ could be identified more easily.

The main challenges of indexing were that each diffraction pattern recorded rarely had more than 2 Bragg vectors present. Therefore, summed diffraction patterns of small areas were required in order to gather enough signal which led to ambiguity. Errors in pattern centering (estimated at $\pm 0.02 \text{ \AA}^{-1}$ [37]) increase the blur in the diffraction spots in summed patterns which make it harder to distinguish between spots from potentially overlapping crystals. To overcome this problem, thickness contrast from HAADF images were used to ensure that summing happened over areas which appeared to be uniform thickness and single particles. In addition, intensities of diffraction vectors should be taken into account by considering dynamical effects to rule out ambiguity that arises from simply looking at vector geometry.

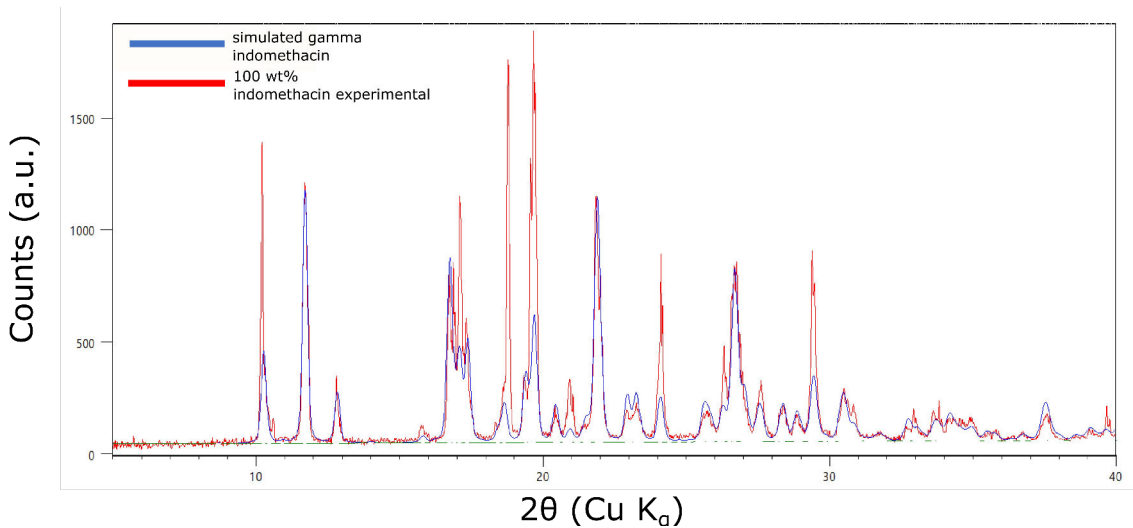


Fig. 3.9 PXRD indicates the presence of the gamma polymorph (CSD number 1180373) as expected.

3.3 Results and Discussion

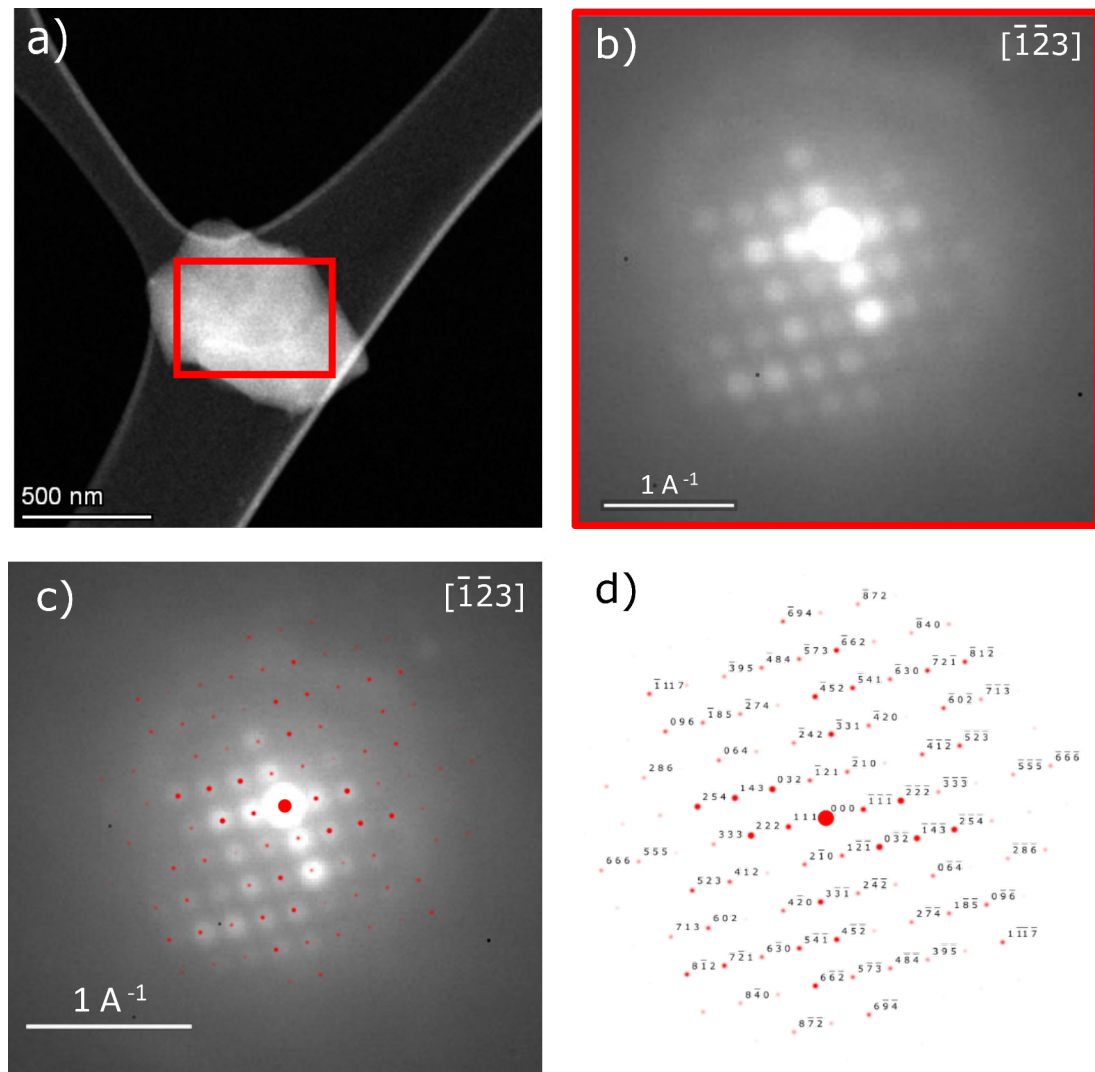
3.3.1 Pure Indomethacin Crystals

Pure crystalline indomethacin samples were initially investigated with the aim of confirming which polymorph was present in the powder. This powder was then used to synthesise the ASD.

PXRD results indicate that the stable γ polymorph was the major component of the pure indomethacin powder. Simulated XRD patterns from crystal structures of indomethacin polymorphs were overlaid on the experimental data (as shown in Figure 3.9) to show a good fit. This is as expected as this is the most stable form of the drug. In SED data, results concurred with PXRD results. Individual crystallites were successfully indexed to the γ polymorph (as shown in Figure 3.10).

3.3.2 Indomethacin-PVP ASDs

Differential scanning calorimetry (DSC) results indicate that ASD samples between 20 wt% and 50 wt% were amorphous as seen by the lack of any sharp peaks in the data shown in Figure 3.11. The slight broad hump peaking at around 100 °C is likely due to water content within the samples. DSC on pure PVP revealed that this was the source of moisture uptake in the ASDs, although this did not result in any unwanted crystallinity that could be observed using XRD or SED. However, new PVP was ordered from Sigma Aldrich to ensure that further samples (60 wt% - 95 wt%), which would become the subject of more intense analysis, did not have unwanted moisture. Pure indomethacin is clearly crystalline, with the sharp peak in Figure 3.11 corresponding to its melting temperature.



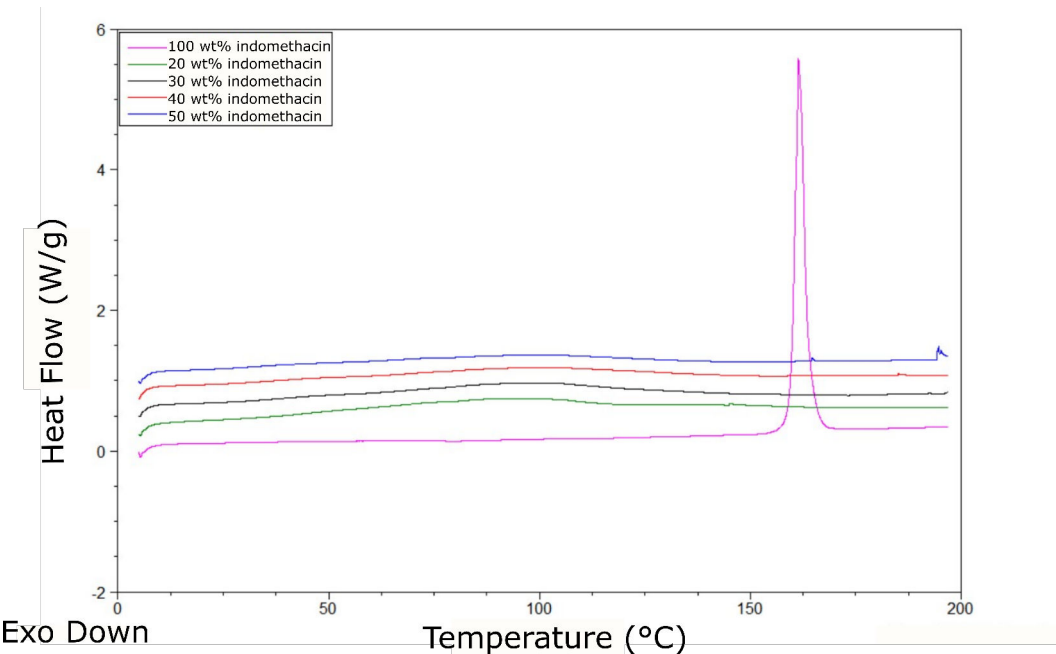


Fig. 3.11 DSC results. The clear spike in pure indomethacin is 165 °C and corresponds to the melting of crystalline material. The lack of peaks in the other samples shows that they are amorphous. The small spike in the 50 wt% peak at 195 °C is likely an anomaly due to sample movement in the heating pan.

PXRD results indicate the amorphous nature of the dispersions from 20 wt% - 70 wt%. As shown in Figure 3.12, there is a change from amorphous material to crystallinity between 70 wt% and 85 wt%. This indicates that the solubility limit of indomethacin in PVP lies within this range which is not inconsistent with Yoshioka [113] and Mohapatra [66], both of whom had synthesised their samples via rotary evaporation.

However, samples at 85 wt% and 95 wt% seem to be only semi-crystalline in nature because of the low intensities of any crystalline peaks. In addition, there is an obvious broad amorphous curve still present under the peaks. When comparing the crystallinity observed in 100 wt% samples to the 85 wt% and 95 wt% samples (shown in Figure 3.14), it is observed that the crystallinity in the samples is not the same as that seen in the pure indomethacin powder. Therefore, at least one new crystal structure has been formed in the synthesis process which is not γ indomethacin. Characteristic peaks between 0 - 15 $^{\circ}$ 2θ were found at: 4.1 $^{\circ}$, 5.3 $^{\circ}$, 6.1 $^{\circ}$, 7.4 $^{\circ}$, 8.3 $^{\circ}$, 10.6 $^{\circ}$, 12.2 $^{\circ}$, and 12.4 $^{\circ}$. Comparison of this unique set of low angle characteristic peaks could not be easily matched to any of the well-known polymorphs of indomethacin (values for these polymorphs are shown in Figure 3.13). With the lowest peak being observed at 4.1 $^{\circ}$ which corresponds to a unit cell of ca. 20 Å, there was a possibility that the structure formed was a co-crystal. However, after a more extensive literature search, a match was found to a

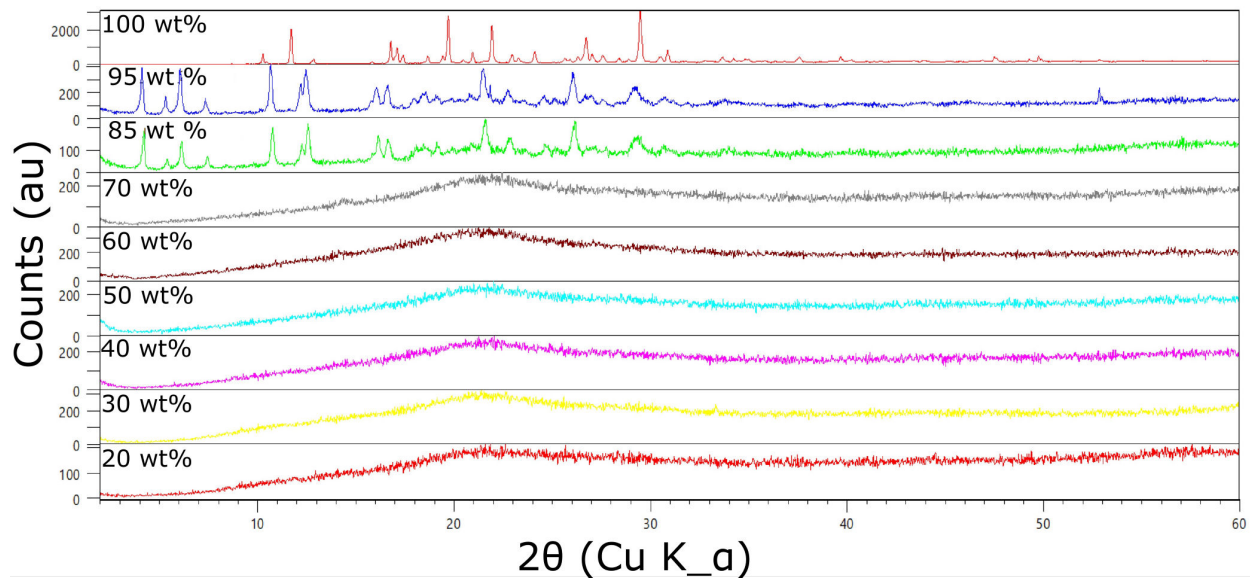


Fig. 3.12 XRD traces of all the samples synthesised. A clear change of crystallinity between 70 wt% and 85 wt% suggesting the solubility limit lies within this range which concurs with [66]. Figure 3.14 shows the change in crystallinity between 85 wt% to 100 wt% in more detail.

XRPD	
solid state form	unique diffraction peak positions ($^{\circ}2\theta$)
amorphous	NA
α	7.0, 8.5, 11.6, 12.0, 14.0, 8.0
γ	10.2, 11.8, 17.0, 19.9, 21.9
δ	9.6, 10.5, 11.3, 13.0, 14.9
ζ	6.5, 11.0, 11.8, 12.8, 14.4, 16.4
η	9.1, 9.3, 12.2, 18.2, 20.5

Fig. 3.13 Characteristic XRD peaks from the known polymorphs of indomethacin. These did not match our results. Figure reproduced from [101].

polymorph discovered using XRD by Duong et al., which they coined the τ polymorph [104]. Their results are shown in Figure 3.15 and characteristic peaks were found at 4.1° , 5.4° , 6.0° , 7.4° , 8.2° , 10.6° , and 12.3° [104]. However, only one peak was observed at 12.3° , whereas 2 distinct peaks were observed in our data at 12.2° and 12.4° . They had also attempted Rietveld refinement on the structure with limited success. Further structure solution and refinement was prohibited by difficulties in isolating the polymorph for XRD. However, lattice parameters and crystal symmetry were proposed. Due to the novel nature of the τ polymorph, a full experimental XRD dataset was not published making it challenging to account for all the peaks observed in our experimental XRD data, and therefore to identify whether τ was the only polymorph present in the sample from XRD.

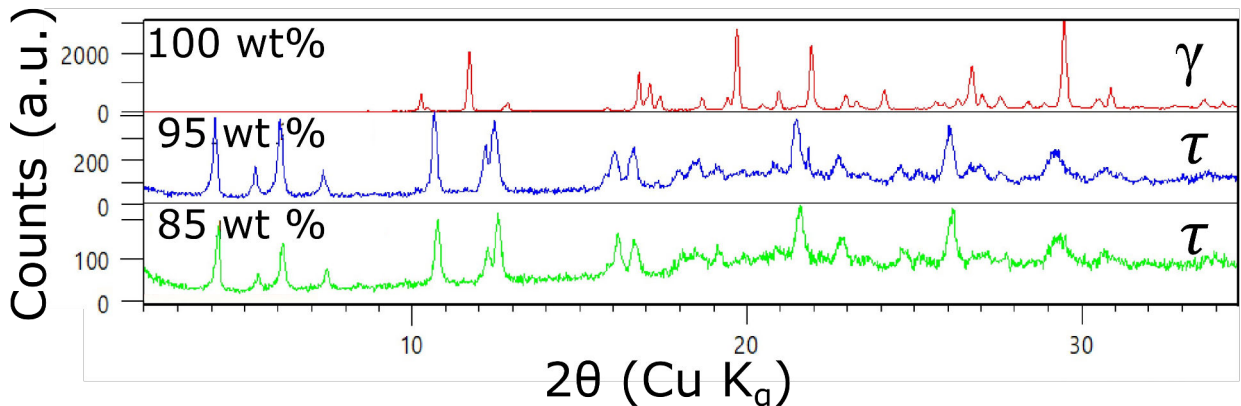


Fig. 3.14 The 85 wt%, 95 wt% indomethacin-PVP ASD XRD traces match the τ polymorph, whilst the 100 wt% indomethacin XRD trace shows the change to the γ polymorph.

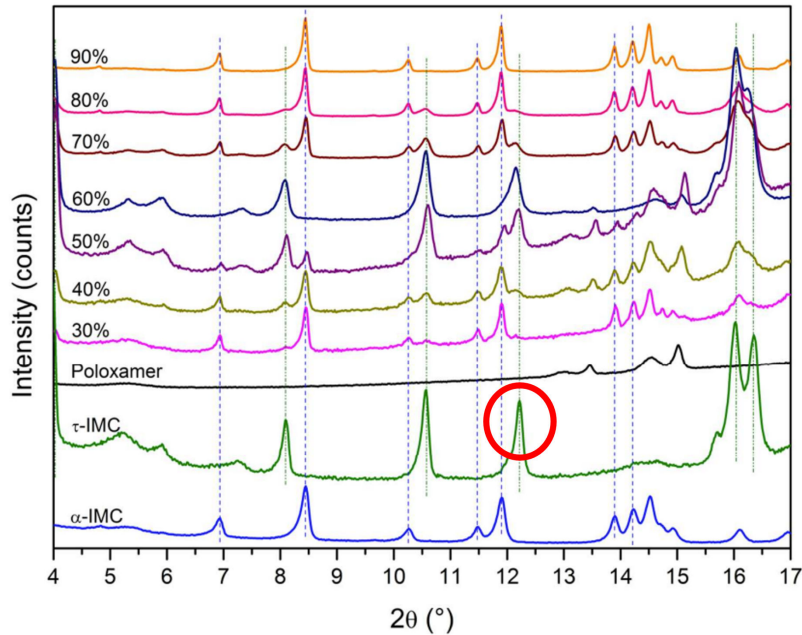


Fig. 3.15 The characteristic XRD peaks in our data match the τ polymorph XRD trace from results by Duong et al. [104]. Only one peak is observed at 12.3° (circled in red), whereas our results for the τ polymorph in Figure 3.14 show 2 clear peaks at 12.2° and 12.4° .

Furthermore, as described by the Scherrer equation, smaller crystallite sizes lead to broadening of crystal peaks in PXRD.

$$d = \frac{k \lambda}{\beta \cos \theta} \quad (3.5)$$

where d is the crystallite size, λ is the wavelength of illuminating irradiation, β is the FWHM of the X-ray peak, θ is the diffraction angle, and k is a constant. These broadened peaks can easily become indistinguishable amongst the amorphous halo if the sample contains varying degrees of crystallinity. It would therefore be difficult to establish the presence of nanocrystalline areas of different polymorphs without the use of SED. However, using information from attempts at Rietveld refinement by Luong et al., a unit cell was created in CrystalMaker such that the geometrical positions of diffraction reflections under the τ polymorph could be compared with other polymorphs within SED data.

SED data in particles which were amorphous were noted but then dismissed upon initial analysis. Whilst it may have been possible to carry out Pair Distribution Function analysis (PDF), this work fell out of the current scope of the project. Particles in 20 wt% - 70 wt% indomethacin samples appeared amorphous (an example is shown in Figure 3.16) under SED which is concurrent with XRD results.

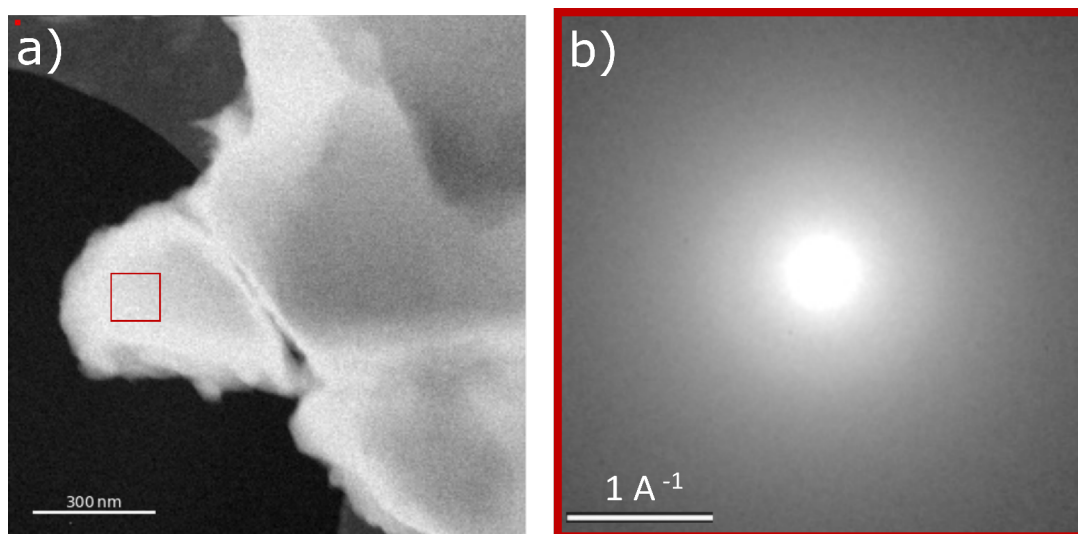


Fig. 3.16 SED data from the 50 wt% ASD. a) the morphology of the particles suggest they are unlikely to be crystalline b) a summed diffraction pattern confirms this.

In the 85 wt% and 95 wt% samples, varying levels of crystallinity were seen; changing from particle to particle. Without the full structure solution of the main source of crystallinity in the sample (the τ polymorph), intensities of simulated diffraction patterns were not accurate so any indexing was limited. However it was possible to demonstrate a convincing fit of certain data to the δ polymorph (Figure 3.17) which did not fit geometries corresponding to the trial τ structure. The HAADF image shown in Figure 3.17 a) was used to ensure that only signal from the most uniform area of the crystallite was taken to create the summed diffraction pattern. The pattern in Figure 3.17 b) was indexed using the methods described in Section 3.2.2 as the δ polymorph parallel to the [3 -4 -1] direction vector. This

result highlights the unique ability of SED to detect local variations in crystallinity. In comparison, PXRD results were only able to confirm the presence of the τ polymorph.

In Figure 3.18, two regions of distinct crystallinity were observed. However, indexing of these patterns is hard and must be approached with extreme caution. In particular, the contrast in the HAADF (Figure 3.18 a)) shows that signal taken from the green area may include two crystals which are likely to be in different orientations. This explains the geometrical irregularity between diffraction vectors seen in pattern c). The summed diffraction pattern b) from the red area shows interesting overall contrast. The X shape is reminiscent of a helical structure and may imply that there is some twisting present along the crystal. A similar particle, shown in Figure 3.19 also showed a similarly X-shaped diffraction pattern. The crystals appeared to be continuously curved towards the right hand side of the image which would imply a degree of twisting throughout the crystal. The majority of organic crystals feature out-of-plane components of their bonds. As a result, there is a geometrical frustration that drives twisting even with single crystals. However, any twisting present would mean that summed diffraction pattern contain information from crystal planes at different degrees of the twist, which prohibits any indexation.

In Figure 3.20, analysis revealed interesting variation in crystallinity along the same particle. As shown in Figure 3.20 a), HAADF contrast indicates that this is a single particle. In addition, its rod-like nature suggests it is a single crystallite. However, summed diffraction patterns from two different areas lengthways along the crystal show different degrees of crystallinity. The highlighted area in red seems primarily amorphous, as shown in Figure 3.20 b). However, Bragg spots are much clearer in the summed diffraction pattern corresponding to signal from the lower half of the particle, as shown in Figure 3.20 c). VDF contrast also highlights this difference, with d) seeming to show an abrupt discontinuation of diffraction contrast alluding to an interface within the particle itself. One possible explanation for this feature is that this crystal has grown from the larger cluster above it. The bottom half of the particle would have grown first, and may have therefore had more time to crystallise whilst the top half still remains disordered. However, without an in-situ experiment, insight into crystallisation mechanisms can only be speculative.

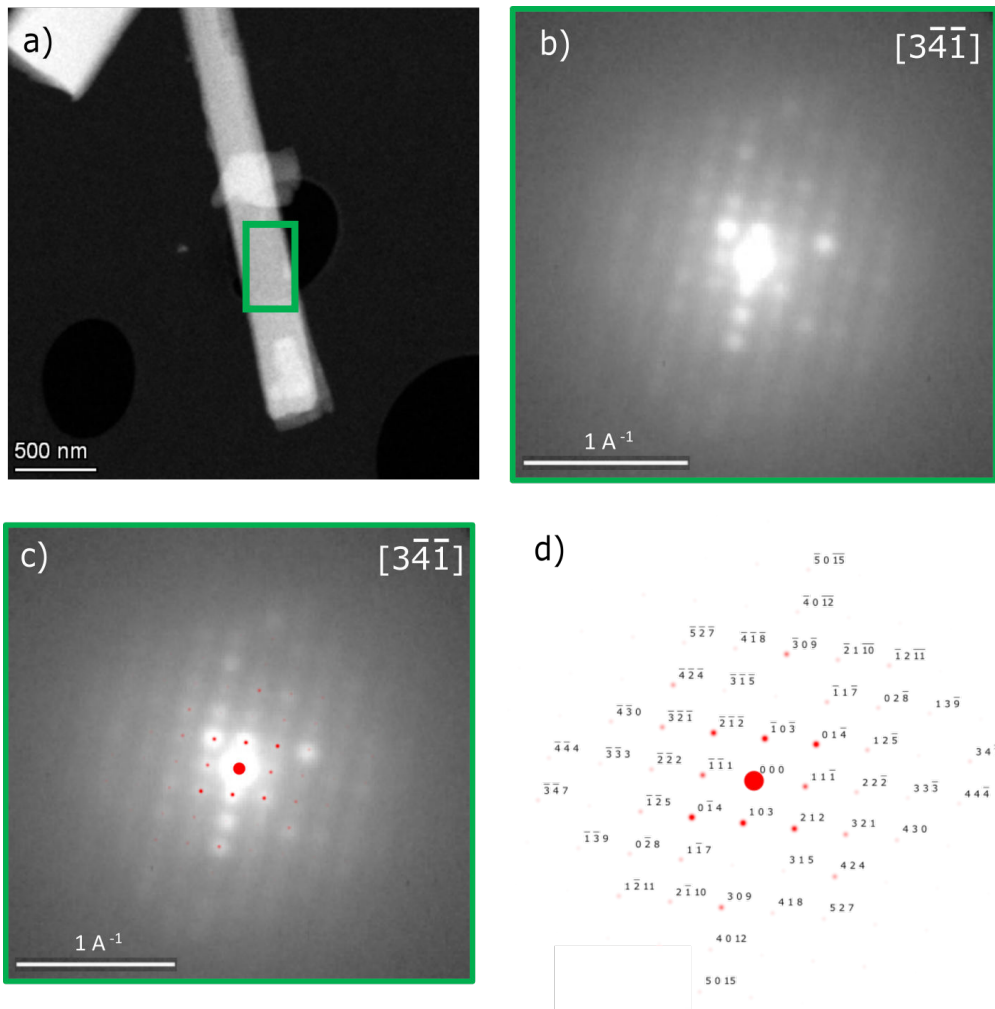


Fig. 3.17 95 wt% indomethacin sample indexed to δ polymorph. Although τ is prevalent in XRD data, δ indomethacin is observed on a local scale. a) The rod-like particle of interest. b) The summed diffraction pattern from the area highlighted in a). c) The fit of the indexed pattern to the experimental pattern. d) The labelled pattern.

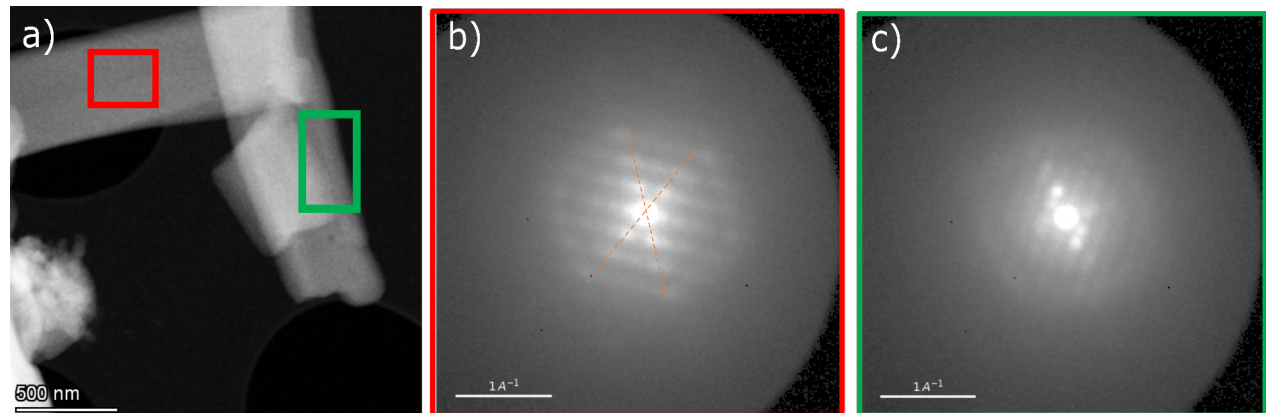


Fig. 3.18 95 wt% indomethacin sample. 2 distinct regions of crystallinity. b) and c) are summed patterns from the coloured regions indicated in a). The orange cross in b) highlights X-shaped contrast reminiscent of a helical structure.

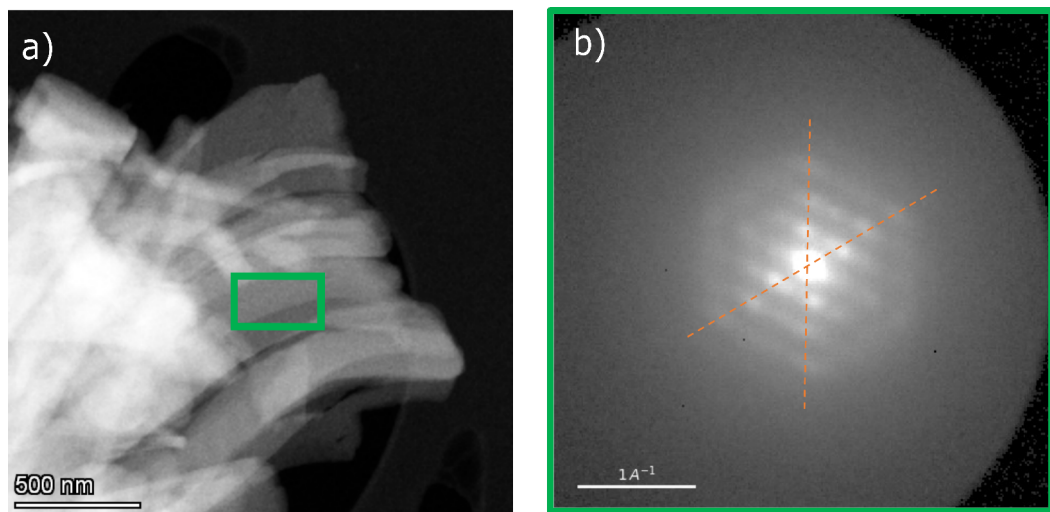


Fig. 3.19 95 wt% indomethacin sample. b) shows the summed diffraction pattern from the area highlighted in a). There is a similar X-shaped contrast as seen in Figure 3.18b) which is reminiscent of a helical structure.

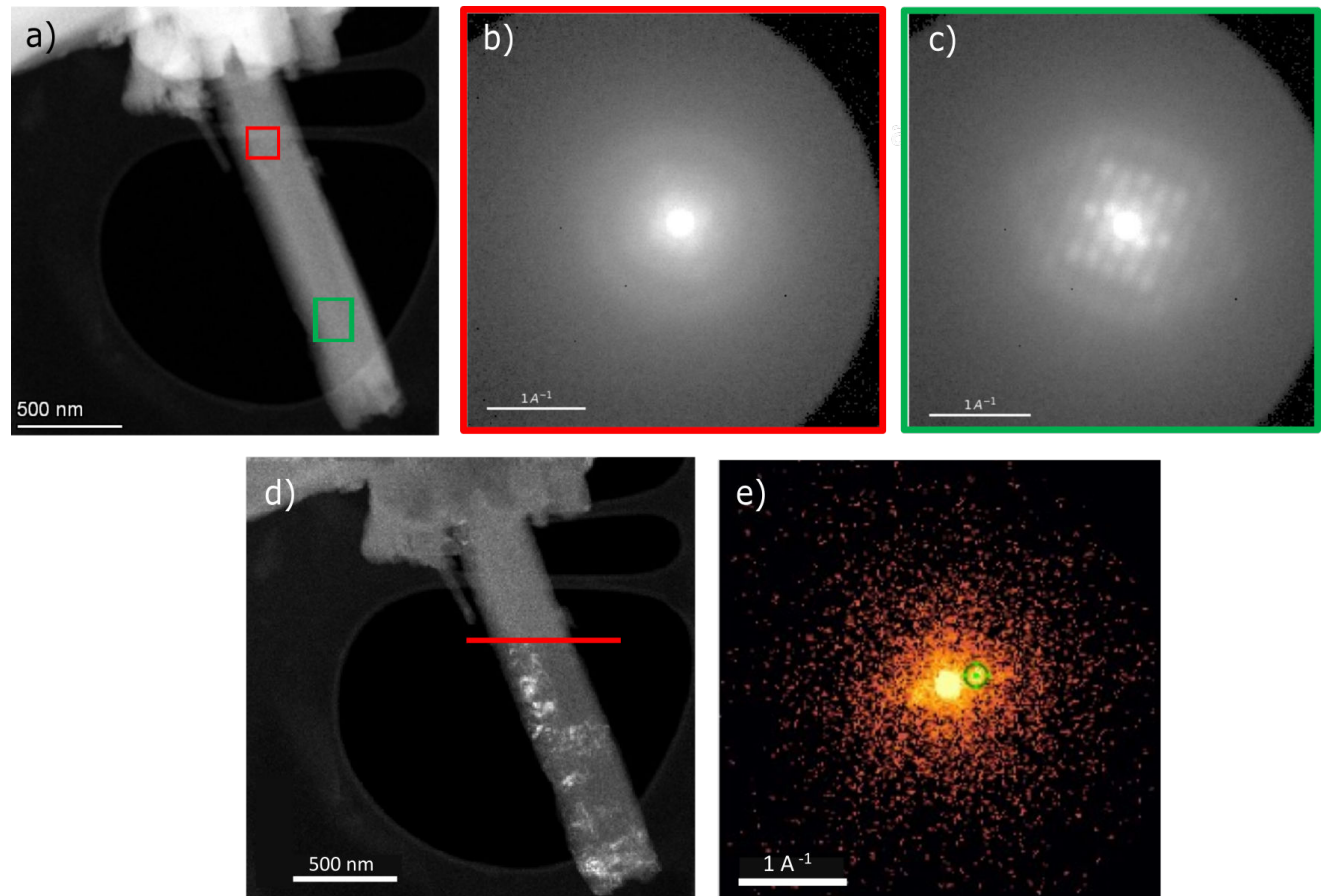


Fig. 3.20 85 wt% particle shown in a) with varying levels of crystallinity along its length. b) indicated the top half of the crystal is amorphous, whilst c) shows clear crystallinity in the bottom half. This is further confirmed by use of VDFs. A virtual aperture shown in e) is used to form the VDF in d). The diffraction contrast shows a higher degree of crystallinity in the bottom half of the particle.

Identifying Contaminants

A typical EDX scan is shown in Figure 3.22. The majority of particles had the expected Cl peak which is the marker in the indomethacin molecule. However, some particles in certain samples lacked the Cl peak and had Ca and S peaks as shown in Figure 3.21. These particles were also highly crystalline despite being present in the 20 wt% indomethacin sample and leading to the conclusion that it was contaminant. The source of the contaminant is believed to be from the dessicator because the dessicant used was anhydrous calcium sulphate. Upon storage, the dessicator was pumped down, possibly causing nanoparticles of the dessicant to fly up and stick to grids. After this discovery, grids were kept in sealed grid boxes wrapped in parafilm. The presence of nanocrystallinity (in the form of contamination) was not detected by XRD, and so these results, although not relevant to the investigation, are concurrent with the hypothesis that SED is much more sensitive to local areas of crystallinity than XRD.

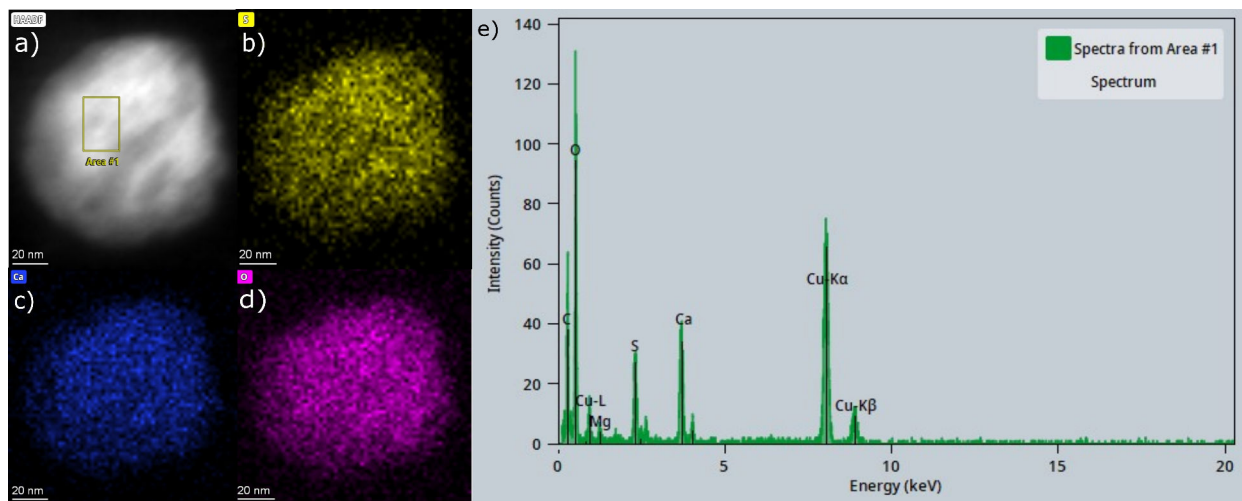


Fig. 3.21 Contaminant particles in the sample were CaSO_4 from the dessicant which led to ‘red herring’ crystallinity. Ca and S peaks are strongly present in this particle. The image streaking indicates signs of astigmatism, caused by changing the optics immediately after SED acquisition to obtain EDX data. However, the image resolution in this scenario is not important to any major results.

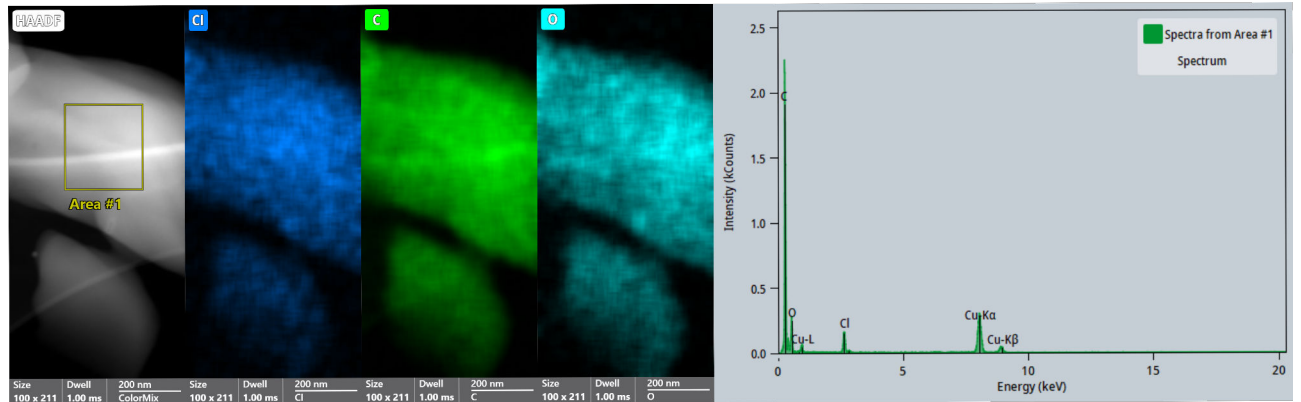


Fig. 3.22 A typical EDX scan acquired at $1 \mu\text{s}$ dwell time for around 2 minutes with the aim of confirming the presence of indomethacin.

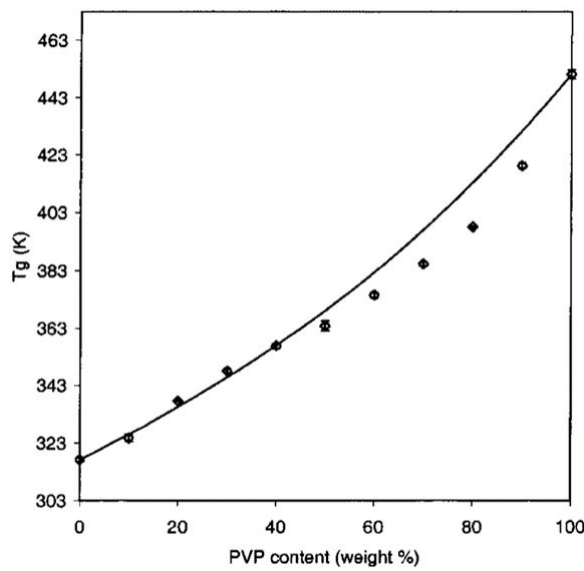
3.3.3 Varying Reported Solubility Limits

Although ASDs can be made through a wide variety of methods, the exact conditions of formation has an effect on the levels of crystallinity observed in the sample. Previous results from within the group (described in Section 3.1.3) indicate that a 70 wt% indomethacin-PVP solid dispersion should be crystalline as measured by XRD. However, the results presented here are not in line with this finding, as the XRD results shown in Figure 3.12 indicate a bulk amorphous sample at 70 wt%. The differing levels of observed crystallinity can likely be attributed to small differences in the manufacturing method and by considering the varying T_g for samples with varying percentages of indomethacin and PVP. The Gordon-Taylor equation can be used to estimate the T_g of a binary mixture by assuming it to be the weighted averages of the free volumes contributed by each component [113].

$$T_{g, \text{mix}} = \frac{[(\omega_1 T_{g1}) + (K\omega_2 T_{g2})]}{[\omega_1 + (K\omega_2)]} \quad (3.6)$$

where T_{g1} , T_{g2} , and $T_{g\text{mix}}$ are the glass transition temperatures of the 2 separate components, and then the mixture, whilst ω_1 , ω_2 are the weight fractions of each component. K is a constant which can be approximated based on the densities of each component. This model assumes that the mixture is a binary mixture although in reality more complex formations may have formed.

The 70 wt% samples from Section 3.1.3 which had been made in a vacuum furnace at 50 °C - 80 °C for 48 hours were crystalline, whereas the 70 wt% samples made via rotary evaporation over a water bath of 40 °C (for around 20 minutes) were still amorphous. Using the Gordon-Taylor relation, the T_g of 20 wt% samples is predicted to be around 105 °C, whilst the T_g of 95 wt% samples is as low as around 25 °C (as shown in Figure 3.23). Therefore, relatively small deviations in manufacturing temperature within the solvent based-evaporation method fall within the range of possible T_g values which will have



try adding my own data points to this when I measure in future

Fig. 3.23 The solid line shows the predicted T_g from the Gordon Taylor Equation. Crowley et al. measured the data points shown. Deviation from predictions occur likely due to non-ideal mixing of the API and polymer [19].

significant effects on bulk crystallinity. The solubility results presented in this work are in line with Mohapatra (shown in Figure 3.24) [66] and Yoshioka [113] which both use rotary evaporation.

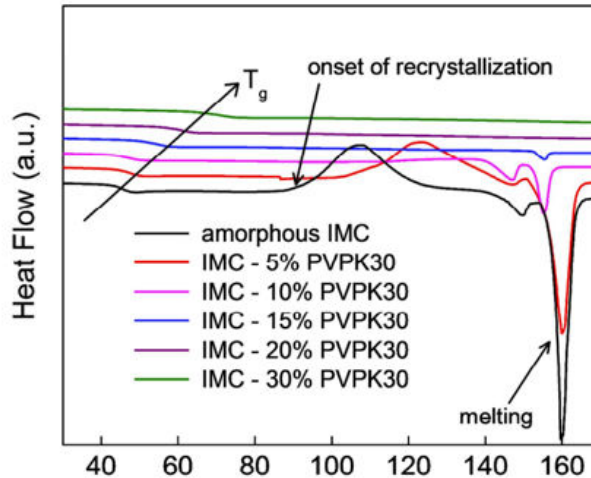


Fig. 3.24 Results from Mohapatra et al. [66] suggest that the solubility limit of indomethacin in PVP lies near 80 wt% indomethacin, unlike the 40 wt% reported by Knopp et al. [50].

3.4 Improving the work

3.4.1 Further XRD analysis

Despite this investigation being primarily focussed on electron diffraction techniques, the XRD data could be further analysed to retrieve results which might complement the investigation. For example, the amount of crystallinity compared to the level of amorphous material could be extracted by considering the area under the broad amorphous curve. However, there will be difficulties due to ambiguity about whether broad features are a result of amorphous material or nanocrystallinity- both of which have been shown to be present using SED.

3.4.2 Increasing Data Quality

Many observed particles in 85 wt% and 95 wt% samples were clearly crystalline to some extent. However, the spacing of some of the reflections on the detector overlap which hinder the resolution to see any finer spots which correspond to larger d -spacings. To improve this, the camera length should be increased in future experiments. An aim would be for the radius of the detector to correspond to about 1 \AA^{-1} . In addition, a smaller condenser aperture should be used to reduce the convergence angle which will help to make the radius of the Bragg discs smaller so that they don't overlap.

Furthermore, the Spectra 300 is a newly installed microscope, and would benefit from some more investigation into optimum acquisition conditions. In particular, the operation of the Medipix detector could be taken into greater consideration. Energy from elastically scattered electrons is dissipated across several pixels on the detector. This energy dissipation is greater at higher acceleration voltages, which means that thick pixel direct electron detectors such as the Medipix operate best at low accelerating voltages. However, in this work the Medipix was operated at 300 kV to minimise beam damage effects on the specimen. This raises the question of finding an accelerating voltage which optimises the trade-off between these two considerations. In addition, the threshold of energy measured in an individual pixel can be changed to make the detector more or less sensitive to this energy spread. The optimum threshold value for different accelerating voltages are parameters yet to be explored which may be the reason that some diffraction spots acquired in this work appear blurred. Therefore, optimisation of data acquisition conditions is still open to exploration in the next stages of this work. An initial calculation of the MTF on the Medipix² indicates a poor performance with room for improvement, as shown in Figure 3.25.

²The script for this was provided by Armand Beche at the Quantitative Electron Microscopy School, 2022.

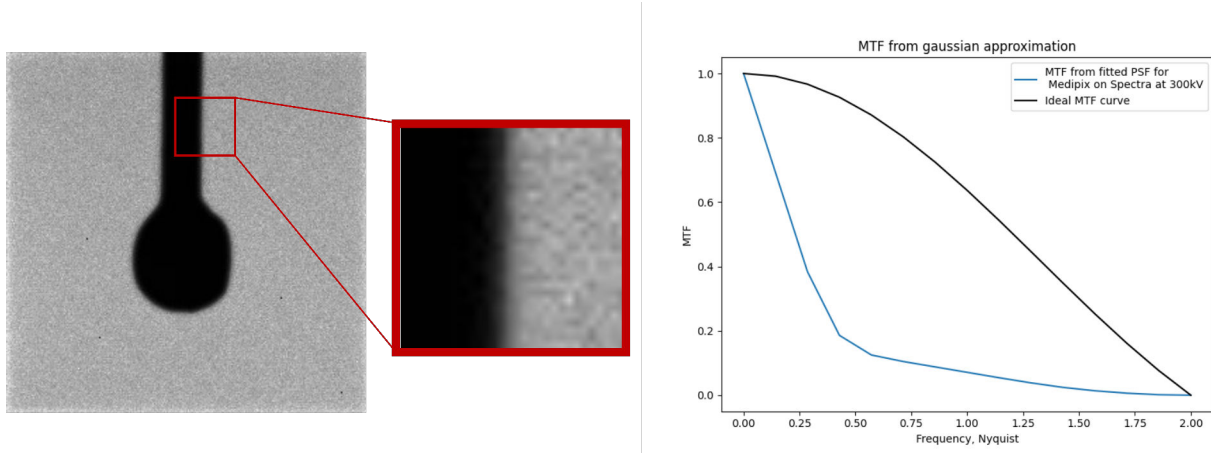


Fig. 3.25 MTF calculated using the knife edge technique [72].

3.4.3 Developing Diffraction Pattern Analysis

Whilst there are template matching algorithms which have been developed for metallic systems with high symmetry [41], [13], the difficulties in indexing organic crystals (described in Section 3.2.2) make any form of automation difficult. In addition, the presence of multiple polymorphs often adds ambiguity, especially when only kinematical intensities were considered. In order for indexing of these systems to become a more straightforward task, precession of the beam may be considered to make the intensities of the diffraction patterns ‘more kinematical’ [65]. Combined with peak finding algorithms, this might open the door for application of machine learning techniques to be applied to organic data.

3.5 Conclusion and Outlook

In this project, an amorphous solid dispersion of indomethacin and PVP was investigated using XRD and SED. Samples across a range of compositions were made via rotary evaporation. The solubility limit was found to be between 70 - 85 wt%. SED gave an insight into the nature of observed crystallinity. In particular, diffraction patterns were indexed to confirm the presence of polymorphs of indomethacin. The spatial distribution of this crystallinity and the morphology of individual particles was also highlighted. In 85 wt% and 95 wt% samples, the τ polymorph was formed, for which the crystal structure has not yet been solved. This leads to an interesting opportunity to apply 3D-ED techniques to the sample to solve the structure. However, results indicate that caution should be applied. SerialED approaches are not likely to be reliable given the range of polymorphs within the sample which would make reconstructing a full dataset from various particles much more challenging.

Chapter 4

Simulating Dynamical Diffraction

Simulations are important to complement experimental work. Often, a comparison between experimental and simulated images is used to refine and confirm a model. Although the work in this chapter is not fully completed, it has been presented alongside a discussion about motivations for carrying out diffraction simulations in future work.

4.1 Image Simulation Theory

Image simulation is the process by which electron microscopy outputs are calculated by modelling the scattering of the electron beam as it passes through a sample. Simulation plays a key role in interpretation of experimental images due to the loss of phase information (the phase problem). The electrons in the microscope are travelling at a significant percentage of the speed of light meaning that their wavefunction $\psi(\vec{r})$ is therefore described by the Schrödinger equation for fast electrons: [48]

$$\frac{\delta\psi(\vec{r})}{\delta z} = \frac{i\lambda}{4\pi}\nabla^2\psi(\vec{r}) + i\sigma V(\vec{r})\psi(\vec{r}) \quad (4.1)$$

where λ is the relativistic wavelength of the electron, $V(\vec{r})$ is the electrostatic potential of the sample (which will depend on the atoms present and their geometry), where it is assumed that the wave function may be represented by a modulated plane wave.

From this equation, there are two main approaches for finding and propagating solutions: the Bloch wave method, and the multislice method.

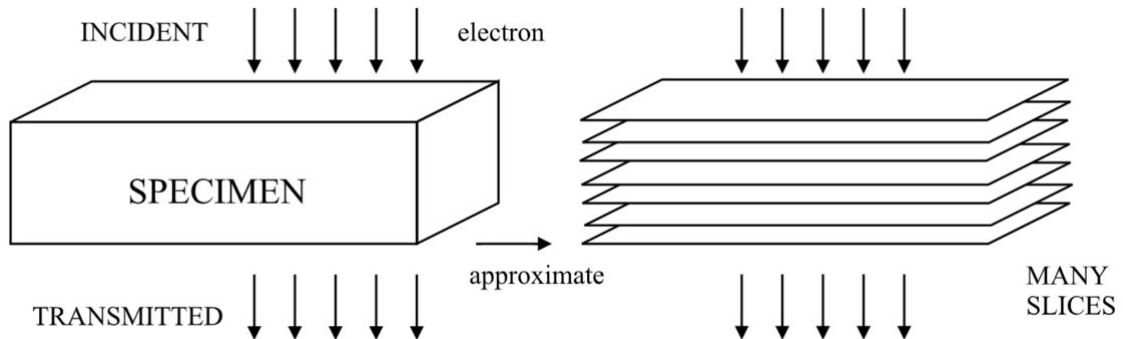


Fig. 4.1 The multislice approach takes thin slices of the specimen. Figure adapted from [48].

The Bloch wave approach assumes a periodic sample. The electron wave function must have the symmetry of the crystal because the electron experiences a periodic potential. The solutions to the Schrodinger equation which obey the crystal symmetry are the Bloch waves [109]. A series of Bloch waves can be used to describe the wavefunction inside the crystalline sample: these are the eigenfunctions of electrons inside the crystal. The more complex a sample, the more components will be required. To find the solutions, an eigenvalue matrix equation is set up. Solving the eigenvalue equation will require computing time which scales with N^3 where N is the number of Bloch waves used. Therefore, the Bloch approach is ideal for small perfect crystals.

The multislice method solves the Schrödinger equation using a numerical integration approach proposed by Cowley and Moodie [18]. The electron wave function is factored into a slowly varying part (that is sampled in real space), and another part which varies with the wavelength. The specimen is divided into many thin layers (x, y planes) and the electron wavefunction at a depth z inside the specimen is repeatedly evaluated, where z is perpendicular to the optical axis, as shown in Figure 4.1. Each slice is thin enough that the electron wave can be approximated as having undergone a simple phase shift (a simple/weak phase object) such that propagation between slices can be determined using Fresnel diffraction [48]. The fast Fourier transform was introduced by Ishizuka et al. in 1977 which increased the computational efficiency of the multislice method [36], thus making multislice a popular method for image simulation. However, the edges of each layer must obey periodic boundary conditions in the plane of the slice. [48]. Multislice is often preferred to the Bloch Wave approach because the use of the discrete Fourier transform provides $N \log(N)$ time complexity. In addition, it is possible to simulate defects, disorder, and partial coherence in samples.

4.2 Motivations: Diffraction Simulation in Organic Crystals

Simulation of diffraction patterns is a key step required in any form of crystal structure determination. As discussed in Chapter 2.3.2, the use of electron diffraction for structure solution poses advantages over XRD for several key reasons. Many complex proteins and small organic molecules are difficult to crystallise into single crystals large enough for XRD. The requirement for crystallisation also hampers the ability to observe any of these compounds of interest in their ‘native’ form, such as in the final product formulation form. However, the majority of structures solved using 3D-ED have firstly already been solved using XRD, and have high R-factors. As a result of the strong dynamical effects in electron diffraction data, there is a requirement to simulate dynamical diffraction effects, not just kinematical simulations. These simulations play an important role in dynamical structure refinement which is crucial to obtaining lower R factors.

MULTEM is a software created by Lobato et al. which implements the multislice method [59]. Many other multislice software also exist, such as μ STEM [87], PRISMATIC [2], abTEM [61]. However, none of these softwares offer small angle tilt electron diffraction simulation. This is necessary for simulating the 3D-ED datasets needed for structure determination.

4.3 Method

The Cambridge Crystallographic Structural Database was used to retrieve cif files of the polymorphs of acetaminophen. Acetaminophen was chosen as a simple small organic molecule on which to test simulations. The most stable polymorph, its monoclinic form, was chosen. The Atomic Simulation Environment library in python [33] was used to read the cif file and create a supercell. From one unit cell of monoclinic acetaminophen (shown in Figure 4.2 a)), a supercell of size 10 x 10 x 10 was created, as shown in Figure 4.2 b). To simulate small rotations, an Euler rotation from the scipy python library [106] was used to rotate the entire coordinate system about the x axis by a given amount. This led to samples similar to the model illustrated in Figure 4.3 b). These coordinates were then exported and fed into MULTEM.

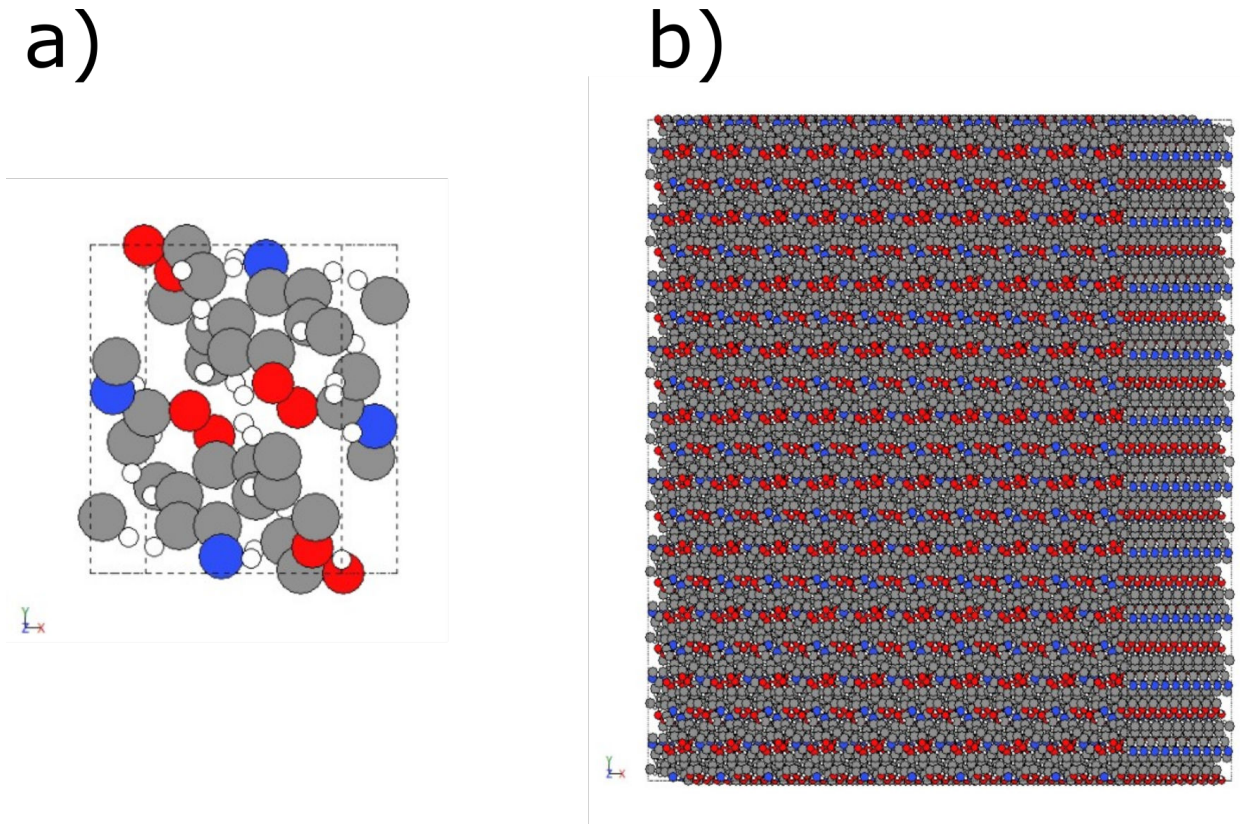


Fig. 4.2 a) a single unit cell of monoclinic acetaminophen, where the grey atoms are C, white atoms are H, blue atoms are N, and red atoms are O. b) making a $10 \times 10 \times 10$ supercell from the unit cell.

MULTEM [59] was used for simulations because of previous experience using the software. The input information required by MULTEM consists of a set of atomic coordinates for every atom in the sample, and parameters to define the operation of the electron microscope. Within MULTEM, the ‘Electron Diffraction’ mode script was adapted to tweak input conditions. An accelerating voltage of 300 kV and convergence angle of 0.5 mrad were used. Aberrations were left as default values.

An additional model was tested whereby coordinates falling outside of a certain boundary were discarded such that the surface of the input model was perpendicular to the direction of beam propagation, shown in Figure 4.3 c). However, the edges of the model were not periodic and odd atoms were placed along the boundary and led to strange geometries and streaking in the patterns which were discarded.

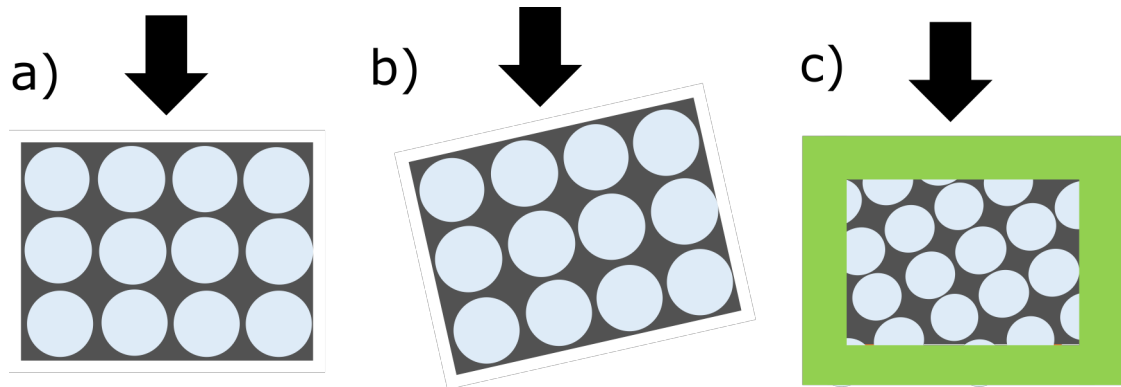


Fig. 4.3 Schematic of how tilting geometries were implemented within MULTEM. The blue circles represent atoms and the black arrow represents the direction of the incoming electron beam. a) Illustrating sample geometry with no tilting. b) Applying an Euler rotation to tilt the sample.

4.4 Results and Discussion

Figure 4.4 shows the results of trial simulations run in MULTEM. Streaking is visible across all the diffraction patterns, indicating that padding or the transverse size of the unit cell is not sufficient to prevent wrap around artefacts. It is unclear why there is lateral streaking in the 0° diffraction pattern. In the rotated patterns, lack of periodicity in the input model boundaries is likely the cause of streaking. The requirements for calculating an edge which is periodic would be to create a specimen extra long in the nonperiodic direction [48]. This geometry is displayed in Figure 4.5. If long enough, this supercell will stop the interfaces from interacting with each other. Padding (shown in green) should also be added to the model. However, for small tilt angles this will require very wide unit cells.

The attempts to simulate a small angle tilt series using a multislice approach was initially unsuccessful due to the geometric challenges associated with the algorithm which requires thin periodic slices. The results presented here support the fact that padding and large transverse super cells are required in order to use multislice for electron diffraction simulation in non zone-axis orientations. However, using a Bloch wave approach would not require these corrections, as random orientations of any lattice are able to be simulated. Although the Bloch wave approach has a time complexity which scales as N^3 , the diagonalisation of the matrix only needs to be done once and diffracted intensities of the beam can be computed for any thickness of the sample. Therefore, it was decided that a Bloch wave approach might be more appropriate, especially given that many of the structures of interest are defect-free. Multislice would still be useful to simulate images of defects.

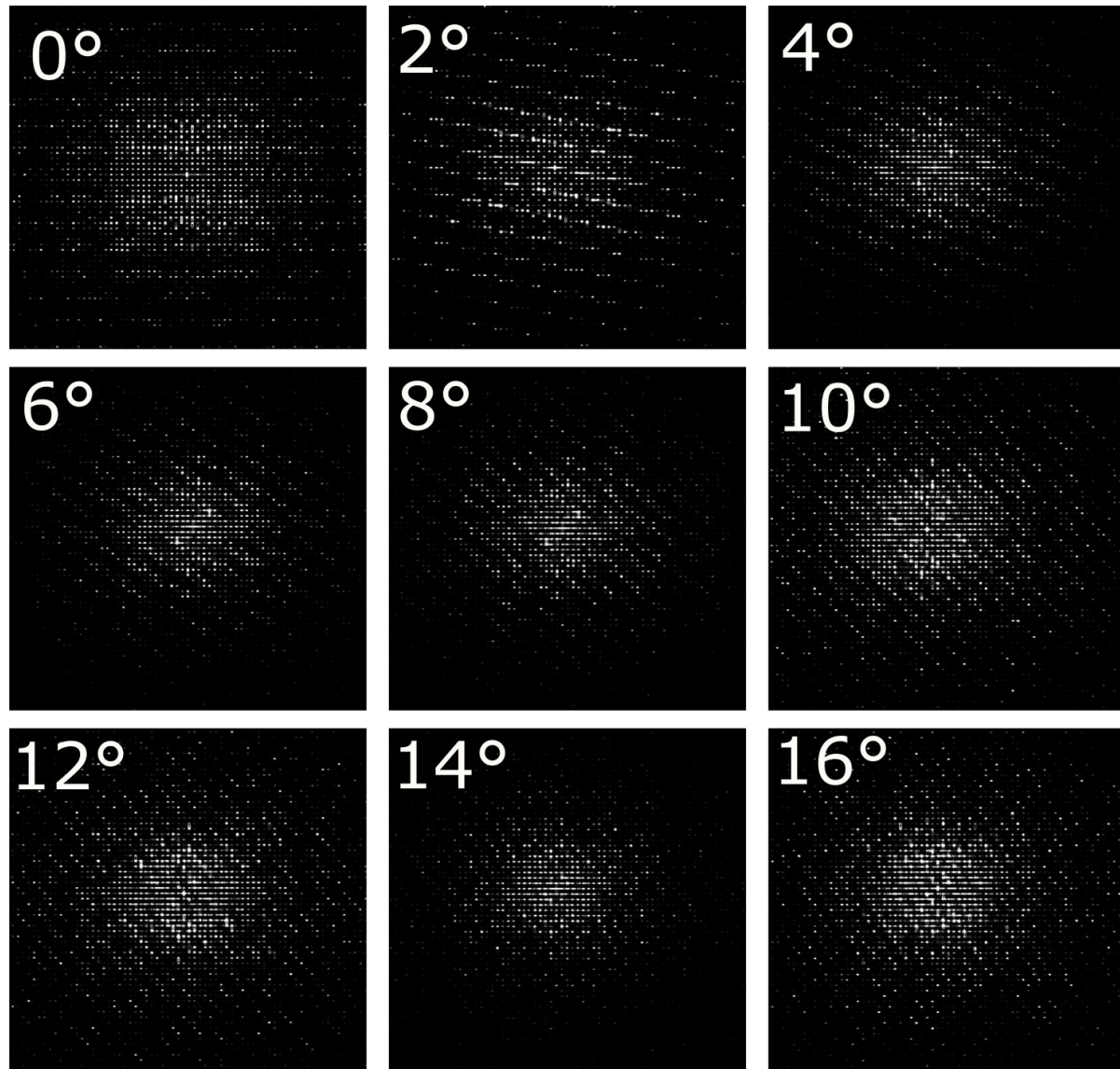


Fig. 4.4 A rotation series generated through MULTEM simulations rotating monoclinic acetaminophen (CSD number 1178858).

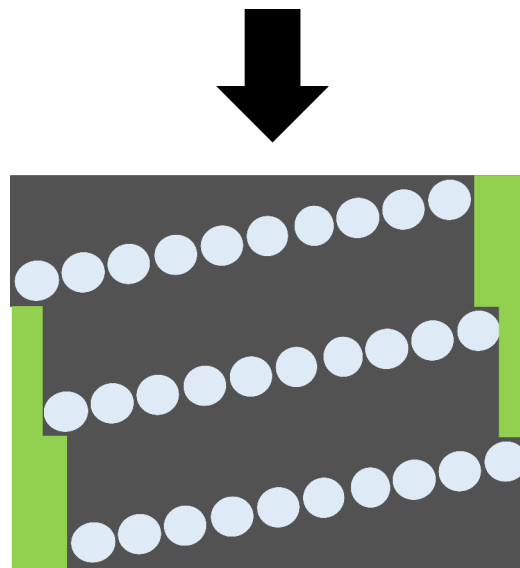


Fig. 4.5 Green represents padding. Periodic boundaries would require padding and large transverse unit cells. The black arrow represents the direction of the incoming electron beam.

4.5 Conclusion

In this chapter, the non-trivial nature of using multislice for small-angle tilt simulation was discussed. Based on the work attempted here, future work likely will be directed towards a Bloch wave approach. However, the inclusion of simulation is still important for the successful development of dynamical refinement processes for crystal structure determination.

Chapter 5

Future Work

5.1 Microstructure and Structure Solution in Solid Form

Solid form samples have been the focus of the investigation carried out so far. The work has revealed areas of interest for further development which are summarised below.

5.1.1 Structure Determination of τ Polymorph

The investigation carried out in Chapter 3 has opened up several questions of interest. The crystal structure of τ indomethacin has not been solved due to difficulties in isolating the polymorphic form. This presents a good opportunity to use 3D-ED to solve the structure. It is planned that the data will be collected on either the Spectra or Krios microscopes within the Wolfson Electron Microscopy Suite. It presents a good opportunity to introduce experimental 3D-ED into the work.

5.1.2 Defect Analysis in Organic Crystals

Whilst investigating Amorphous Solid Dispersions, the construction of VDFs using pyxem demonstrated that there was interesting potential for in-depth defect analysis. Knowledge of defect behaviour and structure in organic crystals is relatively poor. The most prominent experimental work on this subject has been carried out by Jones et al. [42] who explored defect interactions. Studying defects from SED data is difficult because of the inability to choose diffraction conditions to form an image. Traditional methods of tilting the specimen in the TEM which were primarily used to study defects in metals is not feasible due to beam sensitivity of the samples and the relatively ‘urgent’ and automated nature of data acquisition.

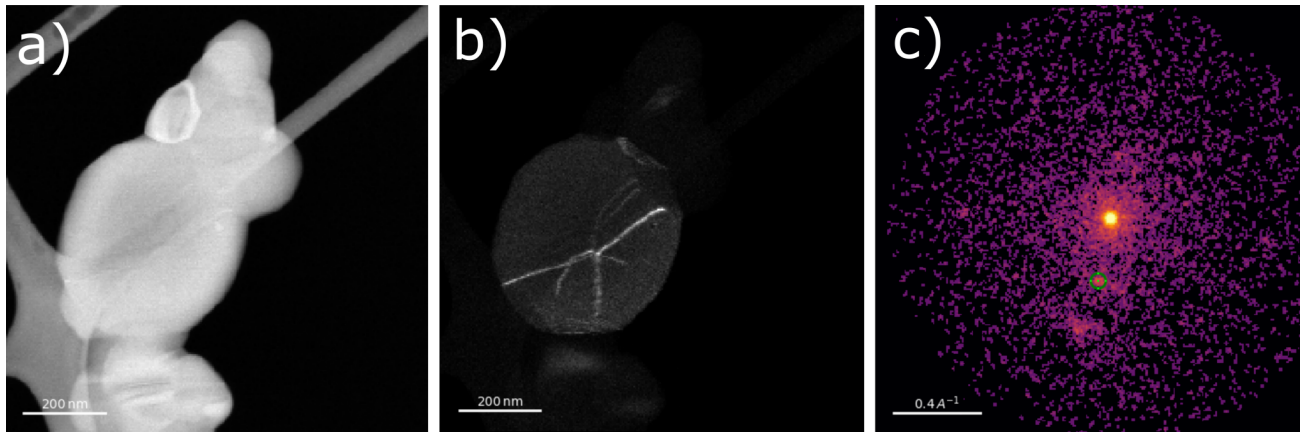


Fig. 5.1 SED data of acetaminophen. a) HAADF image of a cluster of acetaminophen nanoparticles. b) a VDF image showing a suspected dislocation network formed from the virtual aperture shown in c). Data taken by Duncan Johnstone at ePSIC at 300 kV with 2 pA beam current.

Dislocations

Jones et al. have attempted to deduce Burgers vectors of dislocations in *p*-terphenyl but struggled due to only having single micrographs to work from [42]. VDFs from SED may be able to offer much more in depth analysis that could yield interesting results, such as preliminary results shown in Figure 5.1. In addition, there has been work on modelling the potential slip planes of dislocations [56], [75]. This theory may be able to complement potential SED experiments.

5.2 SED of Long Acting Injectables

Aside from oral dosage mechanisms, long acting injectables are another product class designed to administer a slow-release drug. These injectables could contain the drug in several forms such as nanoparticles, microspheres, colloidal dispersions. The drug is a suspension of nanoparticles which makes their sample preparation for TEM relatively easy- the drug can be directly deposited onto a TEM grid. In addition, drug design is becoming increasingly focussed on parenterals and away from solid dosage forms. Therefore, this product class holds plenty of potential for investigation.

5.3 Dynamical Bloch Wave Simulations

Whilst the multislice approach has been attempted in this report, Bloch wave code is available which is the next method to try. For example, Felix is a software written by Beanland et al. which could be adapted for dynamical simulations [6]. As discussed in Chapter 4, simulations are a core part of structure determination using electron diffraction. Dynamical refinement, which will involve use of

dynamical simulations, are important to the success of structure determination. Continuing the work from Chapter 4 will be important to any future projects which will likely involve some degree of structure determination. However, macromolecules are too large to feasibly be dynamically refined. Therefore, some alternative strategies to incorporate dynamical refinement might be explored as well.

5.4 Technique Development

5.4.1 Machine Learning for High Throughput Data Processing

The use of machine learning techniques was approached with caution in this work. Unlike images in real space, strict relationships control the geometry and intensity of Bragg spots in diffraction patterns for which we have mathematical models. Therefore, encoding the high levels of prior knowledge into a machine learning algorithm is timely and perhaps no better than manual analysis. However, the large volumes of data that can be obtained from a small scan area, especially in SED naturally lends itself to a discussion about the potential of further automation within the data analysis. PCA and unsupervised machine learning techniques such as non-negative matrix factorisation were applied to GaAs wires to demonstrate the ability of learning microstructural features in precessed SED data [62]. Extending these techniques to organic systems would have value in several ways. Firstly, scenarios in which multiple crystals cross the beam's path are common. Being able to distinguish between spots within a diffraction pattern would be valuable. Secondly, machine learning would be helpful in the case of SerialED data in samples where several phases are present. A neural network might be able to detect and distinguish between patterns from different phases which would help to build full datasets. Other work by Kaufmann et al. demonstrated the ability for a neural network to determine crystal symmetry from electron diffraction back-scattered diffraction [46].

5.4.2 Precession

Minimising Dynamical Effects in Experimental Data

One of the challenges faced in the work presented in Chapter 3 was the ambiguity arising from diffraction patterns giving the scarcity of Bragg spots observed. Incorporating precession into this (i.e. doing scanning precession electron diffraction, SPED) might be able to help data analysis leading the way to more automated routes for indexing which do not require such intense manual supervision.

Serial Precession Rotation Electron Diffraction

SerialED has opened up the possibility of further development of the technique. One such idea might be ‘SerPED’, serial precession electron diffraction. This would involve precessing the beam whilst acquiring SED data across the sample. Precession will allow for efficient use of dose, which would be essential for beam-sensitive samples where SerialED may not be feasible.

References

- [1] Adams, P. D., Afonine, P. V., Bunkóczki, G., Chen, V. B., Davis, I. W., Echols, N., Headd, J. J., Hung, L. W., Kapral, G. J., Grosse-Kunstleve, R. W., McCoy, A. J., Moriarty, N. W., Oeffner, R., Read, R. J., Richardson, D. C., Richardson, J. S., Terwilliger, T. C., and Zwart, P. H. (2010). PHENIX: A comprehensive Python-based system for macromolecular structure solution. *Acta Crystallographica Section D: Biological Crystallography*, 66(2):213–221.
- [2] Allen, L., D’Alfonso, A., and Findlay, S. (2015). Modelling the inelastic scattering of fast electrons. *Ultramicroscopy*, 151:11–22. Special Issue: 80th Birthday of Harald Rose; PICO 2015 – Third Conference on Frontiers of Aberration Corrected Electron Microscopy.
- [3] Altomare, A., Giacovazzo, C., Grazia, A., Moliterni, G., and Rizzi, R. (2004). Direct Methods Optimised for Solving Crystal Structure by Powder Diffraction Data: Limits, Strategies, and Prospects. *Journal of Research of the National Institute of Standards and Technology*, 109(1):125.
- [4] Bauer, J., Spanton, S., Henry, R., Quick, J., Dziki, W., Porter, W., and Morris, J. (2001). Ritonavir: An Extraordinary Example of Conformational Polymorphism. *Pharmaceutical research*, pages 859–866.
- [5] Bücker, R., Hogan-Lamarre, P., and Miller, R. J. D. (2021). Serial electron diffraction data processing with diffractem and crystfel. *Frontiers in Molecular Biosciences*, 8:415.
- [6] Beanland, R. (2022). GitHub - WarwickMicroscopy/Felix: Felix: Bloch wave method diffraction pattern simulation software.
- [7] Beche, A. (2022). Lecture notes in electron detection, quantitative electron microscopy school.
- [8] Bhujbal, S. V., Mitra, B., Jain, U., Gong, Y., Agrawal, A., Karki, S., Taylor, L. S., Kumar, S., and (Tony) Zhou, Q. (2021). Pharmaceutical amorphous solid dispersion: A review of manufacturing strategies. *Acta Pharmaceutica Sinica B*, 11(8):2505–2536.
- [9] Brázda, P., Palatinus, L., and Babor, M. (2019). Electron diffraction determines molecular absolute configuration in a pharmaceutical nanocrystal. *Science*, 364(6441):667–669.
- [10] Buerger, M. J. (1944). *The photography of the reciprocal lattice*. Murray printing Company.
- [11] Campbell, J., Burkitt, S., Dong, N., and Zavaleta, C. (2020). Chapter 9 - nanoparticle characterization techniques. In Chung, E. J., Leon, L., and Rinaldi, C., editors, *Nanoparticles for Biomedical Applications*, Micro and Nano Technologies, pages 129–144. Elsevier.
- [12] Cattle, J., Hondow, N., Blade, H., Cosgrove, S., Brydson, R. M., and Brown, A. P. (2015). Analysis of Electron Beam Damage of Crystalline Pharmaceutical Materials by Transmission Electron Microscopy. *Electron Microscopy and Analysis Group Conference*.
- [13] Cautaerts, N., Crout, P., Ånes, H. W., Prestat, E., Jeong, J., Dehm, G., and Liebscher, C. H. (2022). Free, flexible and fast: Orientation mapping using the multi-core and GPU-accelerated template matching capabilities in the Python-based open source 4D-STEM analysis toolbox Pyxem. *Ultramicroscopy*, 237:113517.
- [14] Ceska, T., Chung, C.-W., Cooke, R., Phillips, C., and Williams, P. A. (2019). Cryo-EM in drug discovery. *Biochemical Society Transactions*, 47(1):281–293.

- [15] Chasse, T., Conway, S. L., Danzer, G. D., Feng, L., Leone, A. M., McNevin, M., Smoliga, J., Stroud, P. A., and van Lishaut, H. (2022). Industry White Paper: Contemporary Opportunities and Challenges in Characterizing Crystallinity in Amorphous Solid Dispersions. *Journal of Pharmaceutical Sciences*.
- [16] Clabbers, M. T., Gruene, T., Parkhurst, J. M., Abrahams, J. P., and Waterman, D. G. (2018). Electron diffraction data processing with DIALS. *Acta Crystallographica Section D: Structural Biology*, 74(6):506–518.
- [17] Clabbers, M. T. and Xu, H. (2020). Microcrystal electron diffraction in macromolecular and pharmaceutical structure determination. *Drug Discovery Today: Technologies*.
- [18] Cowley, J. M. and Moodie, A. F. (1957). The scattering of electrons by atoms and crystals. I. A new theoretical approach. *Acta Crystallographica*, 10(10):609–619.
- [19] Crowley, K. J. and Zografi, G. (2002). Water Vapor Absorption into Amorphous Hydrophobic Drug/Poly(vinylpyrrolidone) Dispersions. *Journal of Pharmaceutical Sciences*, 91(10):2150–2165.
- [20] Das, P. P., Guzzinati, G., Coll, C., Perez, A. G., Nicolopoulos, S., Estrade, S., Peiro, F., Verbeeck, J., Zompra, A. A., and Galanis, A. S. (2020). Reliable Characterization of Organic Pharmaceutical Compounds with High Resolution Monochromated EEL Spectroscopy. *Polymers*, 12(7):1–11.
- [21] Das, P. P., Mugnaioli, E., Nicolopoulos, S., Tossi, C., Gemmi, M., Galanis, A., Borodi, G., and Pop, M. M. (2018). Crystal Structures of Two Important Pharmaceuticals Solved by 3D Precession Electron Diffraction Tomography. *Organic Process Research and Development*.
- [22] Datta, S. and Grant, D. J. W. (2004). Crystal structures of drugs: advances in determination, prediction and engineering. *Nature Reviews Drug Discovery* 3:1, 3(1):42–57.
- [23] Eggeman, A. S. (2019). Scanning transmission electron diffraction methods. *Acta Crystallographica Section B*, 75(4):475–484.
- [24] Eggeman, A. S. and Midgley, P. A. (2012). Refining structures against reflection rank: an alternative metric for electron crystallography. *Acta Crystallographica Section A*, 68(3):352–358.
- [25] Elder, D. P., Holm, R., and De Diego, H. L. (2013). Use of pharmaceutical salts and cocrystals to address the issue of poor solubility. *International Journal of Pharmaceutics*, 453(1):88–100.
- [26] Evans, P. and McCoy, A. (2008). An introduction to molecular replacement. *Acta Crystallographica Section D: Biological Crystallography*, 64(Pt 1):1.
- [27] Fitzpatrick, S., McCabe, J. F., Petts, C. R., and Booth, S. W. (2002). Effect of moisture on polyvinylpyrrolidone in accelerated stability testing. *International journal of pharmaceutics*, 246(1–2):143–151.
- [28] Gardner, C. R., Walsh, C. T., and Almarsson, Ö. (2004). Drugs as materials: valuing physical form in drug discovery. *Nature Reviews Drug Discovery* 3:11, 3(11):926–934.
- [29] Gemmi, M., Serravalle, E., and Roberti Di Sarsina, P. (2020). Pharmaceutical Nanotechnology A New Method Based on Electron Diffraction for Detecting Nanoparticles in Injectable Medicines. *Journal of pharmaceutical sciences*.
- [30] Groom, C. R., Bruno, I. J., Lightfoot, M. P., and Ward, S. C. (2016). The Cambridge Structural Database. *Acta Crystallographica Section B*, 72(2):171–179.
- [31] Gruene, T., Holstein, J. J., Clever, G. H., and Keppler, B. (2021). Establishing electron diffraction in chemical crystallography. *Nature Reviews Chemistry*.
- [32] Harris, K. D., Tremayne, M., Lightfoot, P., and Bruce, P. G. (2002). Crystal Structure Determination from Powder Diffraction Data by Monte Carlo Methods. *Journal of the American Chemical Society*, 116(8):3543–3547.

- [33] Hjorth Larsen, A., JØrgen Mortensen, J., Blomqvist, J., Castelli, I. E., Christensen, R., Dułak, M., Friis, J., Groves, M. N., Hammer, B., Hargas, C., Hermes, E. D., Jennings, P. C., Bjerre Jensen, P., Kermode, J., Kitchin, J. R., Leonhard Kolsbjerg, E., Kubal, J., Kaasbjerg, K., Lysgaard, S., Bergmann Maronsson, J., Maxson, T., Olsen, T., Pastewka, L., Peterson, A., Rostgaard, C., SchiØtz, J., Schütt, O., Strange, M., Thygesen, K. S., Vegge, T., Vilhelmsen, L., Walter, M., Zeng, Z., and Jacobsen, K. W. (2017). The atomic simulation environment - A Python library for working with atoms. *Journal of Physics Condensed Matter*, 29(27).
- [34] Hou, J., Chen, P., Shukla, A., Krajnc, A., Wang, T., Li, X., Doasa, R., Tizei, L. H. G., Chan, B., Johnstone, D. N., Lin, R., Schülli, T. U., Martens, I., Appadoo, D., Ari, M. S., Wang, Z., Wei, T., Lo, S.-C., Lu, M., Li, S., Namdas, E. B., Mali, G., Cheetham, A. K., Collins, S. M., Chen, V., Wang, L., and Bennett, T. D. (2021). Liquid-phase sintering of lead halide perovskites and metal-organic framework glasses. *Science*, 374(6567):621–625.
- [35] I, A., V, H., E, M., A, L., C, H., J, P., SR, H., and M, G. (2019). The Crystal Structure of Orthocetamol Solved by 3D Electron Diffraction. *Angewandte Chemie (International ed. in English)*, 58(32):10919–10922.
- [36] Ishizuka, K. and Uyeda, N. (1977). A new theoretical and practical approach to the multislice method. *Acta Cryst.*, 33(5):740–749.
- [37] Johnstone, D. N. (2018). *Crystal Cartography : Mapping Nanostructure with Scanning Electron Diffraction (Doctoral thesis)*. PhD thesis, University of Cambridge.
- [38] Johnstone, D. N., Copley, R. C. B., Graves, R. G., Brum, J., and Midgley, P. A. (2019a). Multidimensional Electron Diffraction-Microscopy of Cabotegravir Nanocrystals. *Microscopy and Microanalysis*, 25(S2):1942–1943.
- [39] Johnstone, D. N., Crout, P., Laulainen, J., Høgås, S., Martineau, B., Bergh, T., Smeets, S., Collins, S., Morzy, J., Ånes, H., et al. (2019b). Pyxem/pyxem: Pyxem 0.10. 0.
- [40] Johnstone, D. N., Firth, F. C. N., Grey, C. P., Midgley, P. A., Cliffe, M. J., and Collins, S. M. (2020a). Direct imaging of correlated defect nanodomains in a metal-organic framework. *Journal of the American Chemical Society*, 142(30):13081–13089. PMID: 32627544.
- [41] Johnstone, D. N., Martineau, B. H., Crout, P., Midgley, P. A., and Eggeman, A. S. (2020b). Density-based clustering of crystal (mis)orientations and the orix Python library. *Journal of Applied Crystallography*, 53:1293–1298.
- [42] Jones, W., Thomas, J. M., Williams, J. O., Gorringe, M. J., and Hobbs, L. (1976). The Characterization of Dislocations in Organic Molecular Crystals by Transmission Electron Microscopy. *Molecular Crystals and Liquid Crystals*, 32(1):39–43.
- [43] Kabsch, W. (2010). XDS. *Acta Cryst.*, 66(2):125–132.
- [44] Karimi-Jafari, M., Padrela, L., Walker, G. M., and Croker, D. M. (2018). Creating Cocrystals: A Review of Pharmaceutical Cocrystal Preparation Routes and Applications. *Crystal Growth and Design*, pages 6370–6378.
- [45] Kariuki, B. M., Serrano-González, H., Johnston, R. L., and Harris, K. D. (1997). The application of a genetic algorithm for solving crystal structures from powder diffraction data. *Chemical Physics Letters*, 280(3-4):189–195.
- [46] Kaufmann, K., Zhu, C., Rosengarten, A. S., Maryanovsky, D., Harrington, T. J., Marin, E., and Vecchio, K. S. (2020). Crystal symmetry determination in electron diffraction using machine learning. *Science*, 367(6477):564–568.
- [47] Kim, Y. C., Min, K. A., Jang, D. J., Ahn, T. Y., Min, J. H., Yu, B. E., and Cho, K. H. (2020). Practical approaches on the long-acting injections. *Journal of Pharmaceutical Investigation*, 50(2):147–157.
- [48] Kirkland, E. J. (2010). Advanced computing in electron microscopy: Second edition. *Advanced Computing in Electron Microscopy: Second Edition*, pages 1–289.

- [49] Knoll, M. and Ruska, E. (1932). Das elektronenmikroskop. *Zeitschrift fur Physik*, 78, pages 318–339.
- [50] Knopp, M. M., Olesen, N. E., Holm, P., Langguth, P., Holm, R., and Rades, T. (2015). Influence of Polymer Molecular Weight on Drug-Polymer Solubility: A Comparison between Experimentally Determined Solubility in PVP and Prediction Derived from Solubility in Monomer. *Journal of pharmaceutical sciences*, 104(9):2905–2912.
- [51] Kolb, U., Krysiak, Y., and Plana-Ruiz, S. (2019). Automated electron diffraction tomography - Development and applications. *Acta Crystallographica Section B: Structural Science, Crystal Engineering and Materials*, 75(4):463–474.
- [52] Koning, R. I., Koster, A. J., and Sharp, T. H. (2018). Advances in cryo-electron tomography for biology and medicine. *Annals of Anatomy - Anatomischer Anzeiger*, 217:82–96.
- [53] KR, M., UJ, G., CJ, E., and JG, S. (2001). Theoretical approaches to physical transformations of active pharmaceutical ingredients during manufacturing processes. *Advanced drug delivery reviews*, 48(1):91–114.
- [54] Kuriyama, A. and Ozaki, Y. (2014). Assessment of active pharmaceutical ingredient particle size in tablets by Raman chemical imaging validated using polystyrene microsphere size standards. *AAPS PharmSciTech*, 15(2):375–387.
- [55] Latychevskaia, T. and Abrahams, J. P. (2019). Inelastic scattering and solvent scattering reduce dynamical diffraction in biological crystals. *Acta Crystallographica Section B, Structural Science, Crystal Engineering and Materials*, 75(Pt 4):523.
- [56] Lei, L. and Koslowski, M. (2011). Mesoscale modeling of dislocations in molecular crystals. *Philosophical Magazine*, 91(6):865–878.
- [57] Lightowler, M., Li, S., Ou, X., Zou, X., Lu, M., and Xu, H. (2022). Indomethacin Polymorph δ Revealed To Be Two Plastically Bendable Crystal Forms by 3D Electron Diffraction: Correcting a 47-Year-Old Misunderstanding**. *Angewandte Chemie International Edition*, 61(7):e202114985.
- [58] Lipinski, C. A., Lombardo, F., Dominy, B. W., and Feeney, P. J. (2001). Experimental and computational approaches to estimate solubility and permeability in drug discovery and development settings. *Advanced Drug Delivery Reviews*, 46(1-3):3–26.
- [59] Lobato, I., Aert, S. V., and Verbeeck, J. (2016). Accurate and fast electron microscopy simulations using the open source MULTEM program. *European Microscopy Congress 2016: Proceedings*, pages 531–532.
- [60] Loftsson, T. and Brewster, M. E. (2010). Pharmaceutical applications of cyclodextrins: basic science and product development. *The Journal of pharmacy and pharmacology*, 62(11):1607–1621.
- [61] Madsen, J. and Susi, T. (2020). abTEM: ab Initio Transmission Electron Microscopy Image Simulation. *Microscopy and Microanalysis*, 26(S2):448–450.
- [62] Martineau, B. H., Johnstone, D. N., van Helvoort, A. T. J., Midgley, P. A., and Eggeman, A. S. (2019). Unsupervised machine learning applied to scanning precession electron diffraction data. *Advanced Structural and Chemical Imaging 2019 5:1*, 5(1):1–14.
- [63] McCoy, A. J. and Read, R. J. (2010). Experimental phasing: Best practice and pitfalls. *Acta Crystallographica Section D: Biological Crystallography*, 66(4):458–469.
- [64] McCusker, L. B. (2017). Electron diffraction and the hydrogen atom. *Science*, 355(6321):136.
- [65] Midgley, P. A. and Eggeman, A. S. (2014). Precession electron diffraction-a topical review. *IUCrJ*.
- [66] Mohapatra, S., Samanta, S., Kothari, K., Mistry, P., and Suryanarayanan, R. (2022). Effect of polymer molecular weight on the crystallization behavior of indomethacin amorphous solid dispersions. *Crystal Growth and Design*, 17:28.

- [67] Mosenon, D. E., Mugheirbi, N. A., Stewart, A. A., and Taylor, L. S. (2018). Nanometer-Scale Residual Crystals in a Hot Melt Extruded Amorphous Solid Dispersion: Characterization by Transmission Electron Microscopy. *Crystal Growth and Design*, pages 7633 – 7640.
- [68] Mullard, A. (2020). 2020 FDA drug approvals. *Nature reviews. Drug discovery*, pages 85–90.
- [69] Murali, R. and Burnett, R. M. (1991). X-ray crystallography of very large unit cells: Current opinion in structural biology 1991, 1:997–1001. *Current Opinion in Structural Biology*, 1(6):997–1001.
- [70] Nannenga, B. L. and Gonen, T. (2019). The cryo-EM method microcrystal electron diffraction (MicroED). *Nature methods*, 16(5):369.
- [71] Nannenga, B. L., Shi, D., Hattne, J., Reyes, F. E., and Gonen, T. (2014). Structure of catalase determined by MicroED. *eLife*, 3:e03600.
- [72] Newbury, A., Helder, D., Lee, D., Viallefont-Robinet, F., van den Bergh, F., Fraisse, R., and Saunier, S. (2018). Comparison of MTF measurements using edge method: towards reference data set. *Optics Express*, Vol. 26, Issue 26, pp. 33625-33648, 26(26):33625–33648.
- [73] Nunes, C., Mahendrasingam, A., and Suryanarayanan, R. (2005). Quantification of crystallinity in substantially amorphous materials by synchrotron X-ray powder diffractometry. *Pharmaceutical research*, 22(11):1942–1953.
- [74] Okamoto, S. (2016). Crystal Structures and Lattice Parameters of Allotropes of the Metallic Elements. *Alloy Phase Diagrams*, pages 763–766.
- [75] Olson, I. A., Shtukenberg, A. G., Kahr, B., and Ward, M. D. (2018). Dislocations in molecular crystals. *Reports on Progress in Physics*, 81(9):096501.
- [76] Palatinus, L. (2022). Lecture notes in electron crystallography, quantitative electron microscopy school.
- [77] Palatinus, L., Brázda, P., Boullay, P., Perez, O., Klementová, M., Petit, S., Eigner, V., Zaarour, M., and Mintova, S. (2017). Hydrogen positions in single nanocrystals revealed by electron diffraction. *Science*, 355(6321):166–169.
- [78] Palatinus, L., Brázda, P., Jelínek, M., Hrdá, J., Steciuk, G., and Klementová, M. (2019). Specifics of the data processing of precession electron diffraction tomography data and their implementation in the program PETS2.0. *Na Slovance*, 2:182.
- [79] Palatinus, L. and Chapuis, G. (2007). SUPERFLIP – a computer program for the solution of crystal structures by charge flipping in arbitrary dimensions. *urn:issn:0021-8898*, 40(4):786–790.
- [80] Parikh, D. M. (2005). Handbook of pharmaceutical granulation technology. *Drugs and the pharmaceutical sciences*, 81.
- [81] Paterson, G. W., Lamb, R. J., Ballabriga, R., Maneuski, D., O’Shea, V., and McGrouther, D. (2020). Sub-100 nanosecond temporally resolved imaging with the Medipix3 direct electron detector. *Ultramicroscopy*, 210:112917.
- [82] Patterson, A. L. (1934). A Fourier Series Method for the Determination of the Components of Interatomic Distances in Crystals. *Physical Review*, 46(5):372.
- [83] Pecharsky, V. K. and Zavalij, P. Y. (2005). Fundamentals of powder diffraction and structural characterization of materials. *Fundamentals of Powder Diffraction and Structural Characterization of Materials*, pages 1–741.
- [84] Peltonen, L. (2018). Practical guidelines for the characterization and quality control of pure drug nanoparticles and nano-cocrystals in the pharmaceutical industry. *Advanced Drug Delivery Reviews*, 131:101–115.
- [85] Pham, T. N., Watson, S. A., Edwards, A. J., Chavda, M., Clawson, J. S., Strohmeier, M., and Vogt, F. G. (2010). Analysis of Amorphous Solid Dispersions Using 2D Solid-State NMR and ^1H T1 Relaxation Measurements. *Molecular Pharmaceutics*, 7(5):1667–1691.

- [86] Pickard, C. J. and Needs, R. J. (2011). Ab initio random structure searching. *Journal of Physics Condensed Matter*, 23(5):053201.
- [87] Rangel DaCosta, L., Brown, H. G., Pelz, P. M., Rakowski, A., Barber, N., O'Donovan, P., McBean, P., Jones, L., Ciston, J., Scott, M. C., and Ophus, C. (2021). Prismatic 2.0 – Simulation software for scanning and high resolution transmission electron microscopy (STEM and HRTEM). *Micron*, 151:103141.
- [88] Reimer, L. and Kohl, H. H. (2008). *Transmission electron microscopy : physics of image formation*. Springer.
- [89] Ricarte, R. G., Lodge, T. P., and Hillmyer, M. A. (2016). Nanoscale Concentration Quantification of Pharmaceutical Actives in Amorphous Polymer Matrices by Electron Energy-Loss Spectroscopy. *Langmuir*, 32(29):7411–7419.
- [90] Ricarte, R. G., Van Zee, N. J., Li, Z., Johnson, L. M., Lodge, T. P., and Hillmyer, M. A. (2019). Recent Advances in Understanding the Micro- and Nanoscale Phenomena of Amorphous Solid Dispersions. *Molecular Pharmaceutics*, 16(10):4089–4103.
- [91] Rius, J. (1999). XLENS, a direct methods program based on the modulus sum function: Its application to powder data. *Powder Diffraction*, 14(4):267–273.
- [92] Ruskin, R. S., Yu, Z., and Grigorieff, N. (2013). Quantitative characterization of electron detectors for transmission electron microscopy. *Journal of Structural Biology*, 184(3):385–393.
- [93] Rychkov, D., Arkhipov, S., Boldyreva, E., and IUCr (2014). Simple and efficient modifications of well known techniques for reliable growth of high-quality crystals of small bioorganic molecules. *urn:issn:1600-5767*, 47(4):1435–1442.
- [94] S, J. and G, V. d. M. (2009). Review: physical chemistry of solid dispersions. *The Journal of pharmacy and pharmacology*, 61(12):1571–1586.
- [95] S, L., H, W., Y, Z., R, Z., Z, W., and J, H. (2021). Solid Form and Phase Transformation Properties of Fexofenadine Hydrochloride during Wet Granulation Process. *Pharmaceutics*, 13(6).
- [96] S'ari, M., Blade, H., Cosgrove, S., Drummond-Brydson, R., Hondow, N., Hughes, L. P., and Brown, A. (2021). Characterization of amorphous solid dispersions and identification of low levels of crystallinity by transmission electron microscopy. *Molecular Pharmaceutics*, 18(5):1905–1919. PMID: 33797925.
- [97] Sawaya, M. R., Rodriguez, J., Cascio, D., Collazo, M. J., Shi, D., Reyes, F. E., Hattne, J., Gonen, T., and Eisenberg, D. S. (2014). Ab initio structure determination from prion nanocrystals at atomic resolution by MicroED. *Janelia Research Campus*.
- [98] Sheldrick, G. and IUCr (2007). A short history of SHELX. *urn:issn:0108-7673*, 64(1):112–122.
- [99] Smalley, C. J., Hoskyns, H. E., Hughes, C. E., Johnstone, D. N., Willhammar, T., Young, M. T., Pickard, C. J., Logsdail, A. J., Midgley, P. A., and Harris, K. D. (2022). A structure determination protocol based on combined analysis of 3D-ED data, powder XRD data, solid-state NMR data and DFT-D calculations reveals the structure of a new polymorph of L-tyrosine. *Chemical Science*, 13(18):5277–5288.
- [100] Smeets, S., Zou, X., and Wan, W. (2018). Serial electron crystallography for structure determination and phase analysis of nanocrystalline materials. *Journal of Applied Crystallography*, 51(5):1262–1273.
- [101] Surwase, S. A., Boetker, J. P., Saville, D., Boyd, B. J., Gordon, K. C., Peltonen, L., and Strachan, C. J. (2013). Indomethacin: New polymorphs of an old drug. *Molecular Pharmaceutics*, 10(12):4472–4480.
- [102] Taylor, G. L. (2010). Introduction to phasing. *Acta Crystallographica Section D: Biological Crystallography*, 66(Pt 4):325.

- [103] Tran, P. and Park, J. S. (2021). Recent trends of self-emulsifying drug delivery system for enhancing the oral bioavailability of poorly water-soluble drugs. *Journal of Pharmaceutical Investigation 2021* 51:4, 51(4):439–463.
- [104] Van Duong, T., Lüdeker, D., Van Bockstal, P. J., De Beer, T., Van Humbeeck, J., and Van Den Mooter, G. (2018). Polymorphism of Indomethacin in Semicrystalline Dispersions: Formation, Transformation, and Segregation. *Molecular Pharmaceutics*, 15(3):1037–1051.
- [105] Vincent, R. and Midgley, P. A. (1994). Double conical beam-rocking system for measurement of integrated electron diffraction intensities. *Ultramicroscopy*, 53(3):271–282.
- [106] Virtanen, P., Gommers, R., Oliphant, T. E., Haberland, M., Reddy, T., Cournapeau, D., Burovski, E., Peterson, P., Weckesser, W., Bright, J., van der Walt, S. J., Brett, M., Wilson, J., Millman, K. J., Mayorov, N., Nelson, A. R. J., Jones, E., Kern, R., Larson, E., Carey, C. J., Polat, I., Feng, Y., Moore, E. W., VanderPlas, J., Laxalde, D., Perktold, J., Cimrman, R., Henriksen, I., Quintero, E. A., Harris, C. R., Archibald, A. M., Ribeiro, A. H., Pedregosa, F., van Mulbregt, P., and SciPy 1.0 Contributors (2020). SciPy 1.0: Fundamental Algorithms for Scientific Computing in Python. *Nature Methods*, 17:261–272.
- [107] Wang, B., Zou, X., and Smeets, S. (2019). Automated serial rotation electron diffraction combined with cluster analysis: an efficient multi-crystal workflow for structure determination. *urn:issn:2052-2525*, 6(5):854–867.
- [108] Willhammar, T., Daicho, K., Johnstone, D. N., Kobayashi, K., Liu, Y., Midgley, P. A., Bergstro, L., and Saito, T. (2021). Local Crystallinity in Twisted Cellulose Nanofibers. *ACS Nano*.
- [109] Williams, D. B. and Carter, C. B. (2009). Transmission electron microscopy: A textbook for materials science. *Transmission Electron Microscopy: A Textbook for Materials Science*, pages 1–760.
- [110] Wishart DS, F. Y. (2021). Drugbank 5.0: a major update to the drugbank database for 2018.
- [111] Woollam, G. R., Das, P. P., Mugnaioli, E., Andrusenko, I., Galanis, A. S., Van De Streek, J., Nicolopoulos, S., Gemmi, M., and Wagner, T. (2020). Structural analysis of metastable pharmaceutical loratadine form II, by 3D electron diffraction and DFT+D energy minimisation. *CrystEngComm*, 22(43):7490–7499.
- [112] Xie, T. and Taylor, L. S. (2017). Effect of Temperature and Moisture on the Physical Stability of Binary and Ternary Amorphous Solid Dispersions of Celecoxib. *Journal of Pharmaceutical Sciences*, 106(1):100–110.
- [113] Yoshioka, M., Hancock, B. C., and Zografi, G. (1995). Inhibition of indomethacin crystallization in poly(vinylpyrrolidone) coprecipitates. *Journal of Pharmaceutical Sciences*, 84(8):983–986.